Natural potential difference induced functional optimization mechanism for Zn-based multimetal bone implants

Jing Xu [a,b,1], Zhenbao Zhang [b,****,1], Jianhui Wang [c,d,e,1], Yuhan Qi [a,b], Xiaohong Qi [c,d,e], Yijie Liang [b], Manxi Li [b], Haixia Li [h], Yantao Zhao [b,f,g,***], Zhuangzhuang Liu [c,d,e,**], Yanfeng Li [a,b,*]

[a] Medical School of Chinese PLA, Beijing, 100039, China
[b] Department of Stomatology, The Fourth Medical Centre of PLA General Hospital, Beijing, 100048, China
[c] Key Laboratory for Advanced Materials Processing, Institute for Advanced Materials and Technology, University of Science and Technology Beijing, Beijing, 100083, China
[d] Beijing Advanced Innovation Center for Materials Genome Engineering, University of Science and Technology Beijing, Beijing, 100083, China
[e] Beijing Laboratory of Metallic Materials and Processing for Modern Transportation, Institute for Advanced Materials and Technology, University of Science and Technology Beijing, Beijing, 100083, China
[f] Senior Department of Orthopedics, The Fourth Medical Centre of PLA General Hospital, Beijing, 100048, China
[g] Beijing Engineering Research Center of Orthopedics Implants, Beijing, 100048, China
[h] Institute of Process Engineering, Chinese Academy of Sciences, Beijing, 100190, China

ARTICLE INFO

ABSTRACT

Zn-based biodegradable metals (BMs) are regarded as revolutionary biomaterials for bone implants. However, their clinical application is limited by insufficient mechanical properties, delayed *in vivo* degradation, and overdose-induced Zn^{2+} toxicity. Herein, innovative multi-material additive manufacturing (MMAM) is deployed to construct a Zn/titanium (Ti) hetero-structured composite. The biodegradation and biofunction of Zn exhibited intriguing characteristics in composites. A potential difference of about 300 mV naturally existed between Zn and Ti. This natural potential difference triggered galvanic coupling corrosion, resulting in 2.7 times accelerated degradation of Zn. The excess release of Zn^{2+} induced by accelerated degradation enhanced the antibacterial function. A voltage signal generated by the natural potential difference also promoted *in vitro* osteogenic differentiation through activating the PI3K-Akt signaling pathway, and inhibited the toxicity of overdose Zn^{2+} *in vivo*, significantly improving bone regeneration. Furthermore, MMAM technology allows for the specific region deployment of components. In the future, Ti and Zn could be respectively deployed in the primary and non-load-bearing regions of bone implants by structural designs, thereby achieving a functionally graded application to overcome the insufficient mechanical properties of Zn-based BMs. This work clarifies the functional optimization mechanism for multimetal bone implants, which possibly breaks the application dilemma of Zn-based BMs.

1. Introduction

Bone defects caused by trauma, infection or tumors can result in severe functional impairment [1]. Additional therapeutic measures should be used to promote bone repair when the bone loss exceeds the body's self-repair ability [2]. The in situ implantation of bone graft

materials at the defect site is an effective strategy for repairing the structure and function of bone [3]. Biomedical metals, including titanium (Ti), tantalum (Ta) and their alloys, have been widely used as bone repair materials, owing to their excellent biocompatibility and mechanical properties [4]. However, their non-degradable nature, insufficiency of antibacterial property, and the risk of stress-shielding, raise many concerns about long-term efficacy. Biodegradable metals (BMs), which can gradually degrade in body fluids, and promote tissue repair through degradation products, have been investigated as promising orthopaedic implants [5]. Among them, zinc (Zn)-based BMs, characterized by the multifunctional properties of biodegradability, antibiosis and osteogenesis, have been investigated for potential applications as screw and plate systems [6], intramedullary needles [7], guided bone regeneration membranes [8], and bone graft materials [9,10], etc. As reported, Zn^{2+} released from Zn degradation could promote bone regeneration by influencing biological processes, such as the transduction of cell signaling, regulation of enzyme activity, and DNA synthesis [11]. Meanwhile, Zn could induce the generation of hydroxyl radicals, thus killing the bacteria through oxidative stress response [12].

However, bone is a heterogeneous material with individualized anatomical morphology and complex porous structure. Conventional casting or forging techniques are difficult to match the Zn-based BMs with bone in the 3D spatial configuration [13]. The additive manufacturing (AM) technology based on laser powder bed fusion (L-PBF), has been used for the fabrication of Zn-based bone implants with customized morphology and porous structure, due to its high precision [14,15]. Xia et al. [16] fabricated pure Zn porous scaffolds by L-PBF technonlogy, and firstly observed the bone regeneration induced by the scaffolds in the rabbit femur defects. Liu et al. [17,18] also fabricated the porous scaffolds of Zn-Mg and Zn-Li alloy via L-PBF, and found that the degradation behavior and biological function of the scaffolds could be modulated by the structural designs. Therefore, Zn-based bone implants fabricated via L-PBF can greatly meet personalized clinical needs, since L-PBF endows the regulation freedom in morphology, structure and performance of the scaffolds. However, the clinical application of Zn-based BMs is limited by some inherent characteristics. Firstly, the insufficient mechanical properties of pure Zn, with a yield strength of 30 MPa and an elongation of 2 % [19], cannot meet the mechanical requirements for bone implants in the load-bearing regions. Despite the yield strengths of Zn-magnesium (Mg) and Zn-lithium (Li) alloys have been increased to 300–400 MPa by element alloying [20], high brittleness remains an issue. Secondly, the complete degradation of Zn alloys was calculated to take 20 months or even longer [21,22], which apparently needs to be accelerated considering that the recovery of bone defects normally requires 3–6 months. Last but not least, the overdose Zn^{2+} released from accelerated degradation of Zn has significant cytotoxicity [23]. Reconciling the dilemma between rapid degradation and overdose-Zn^{2+} toxicity is a challenge in Zn-based BMs.

Hetero-structured composites, which are macroscopically integrated from different components, can integrate the advantages of those components and form new functions through their interaction [24,25]. Sun et al. [26] fabricated a hetero-structured Zn/Mg bimetal composite, which have enhanced yield strength and elongation compared to pure Zn. Interestingly, the degradation rate of this composite was also significantly increased, due to the potential differences between the dissimilar metals, which induced galvanic corrosion. The potential difference that naturally exists within hetero-structured metal composites may be a critical factor for generating new functions in composites. In addition to triggering galvanic coupling corrosion, this natural potential difference can be regarded as an intervening electrical signal. Specifically, this electrical signal can alter the surrounding electrical microenvironment *in vivo* [27]. The transmembrane potential of cells and the distribution or conformation of charged molecules on the cell membrane undergo adaptive changes in response to changes in the extracellular electrical environment [28,29]. These mediators transduce external electrical signals into nuclear transcription, influencing the signal

transduction cascade and thus regulating cellular function [30]. Chen et al. [31] constructed a spark-plasma sintered Ti/Ta bimetal composite, and found that the surface potential difference of the composite is of the same magnitude as the endogenous potential in the human body, which could modulate osteogenic differentiation of mesenchymal stem cells. Given that the integration of dissimilar metals exhibits potential advantages in enhancing mechanical properties, accelerating degradation, and improving osteogenesis. The development of Zn-based multimetal bone implants possibly overcomes the clinical application challenges of Zn.

Multi-material additive manufacturing (MMAM) technology deploying multiple L-PBF systems has been used to fabricate multimetal composites with hetero-structures for industrial applications [32,33]. The functions of these composites can be programmed through the customization of components and structure, and thus achieving functional gradient applications [34,35]. For bone implants, if biometals with excellent mechanical properties and Zn are deployed respectively in the primary and non-load-bearing regions of bone implants using MMAM technology with structural design, such multimetal bone implants are expected to possess both robust mechanical support and the biofunctions of Zn, which can overcome the insufficient mechanical properties of Zn-based BMs. Meanwhile, the natural potential difference between dissimilar metals, as mentioned above, may also enhance the biofunctions of Zn, including accelerated degradation and improved osteogenesis. However, when printing one metal or alloy layer onto a different metal or alloy base via L-PBF, the mismatch in thermophysical and chemical properties can result in interface cracks [36,37] or detachment [38]. The melting and boiling points of Zn are both lower than other common biometals (Ti, Ta, and Mg), respectively 420 and 907 °C [39]. The evaporation of Zn occurs during multimetal co-printing and causes severe issues with poor interface integration. Till now, there is no information on the fabrication of Zn-based multimetal bone implants using MMAM technology. Additionally, the underlying mechanisms of the effects of natural potential differences on the biodegradation and biofunction of Zn-based multimetal bone implants are unclear, and require systematic investigation for detailed elucidation.

In this work, we overcame the technical difficulties of co-printing Zn with dissimilar metals, fabricated Zn/Ti composites with good fusion quality and strong interfacial bonding using MMAM technology, making the firstly reported AM Zn-based multimetal bone implants to date. Before that, the printing itself was optimized through trial and error. Subsequently, the *in vitro* and *in vivo* performances, including mechanical properties, degradation behavior, osteogenic and antibacterial activity of Zn/Ti composites were systematically investigated. The surface potential difference of the Zn/Ti composites was also characterized, and the balanced relationships between the accelerated degradation of Zn and tissue regeneration, focusing on the electrical signals, were systematically studied at multiple levels including genes, cells and tissues. Compared to the single metal, Zn/Ti composites had accelerated degradation, enhanced osteogenic and antibacterial properties. The study reveals the potential mechanism of functional optimization induced by natural potential difference for multimetal bone implants, offering a prospective solution to break the dilemma of clinical application of Zn-based BMs.

2. Materials and methods

2.1. Sample preparation

Pure Ti and pure Zn powders (Fig. S1a), with a particle size distribution ranging from 15 to 53 μm, were prepared using the vacuum inert gas atomization method. The morphology and element distribution of powders were observed by a scanning electron microscope (SEM, Zeiss, Germany) equipped with an energy dispersive spectrometer (EDS, Ametek, USA). Before processing, the powders were dried at 100 °C for

5 h to remove humidity. A L-PBF machine (BLT A300, China) was used to fabricate the pure Ti, pure Zn and Zn/Ti samples under argon protection. The *in vitro* test samples were pre-defined as a disk with φ10 mm × 2 mm, and *in vivo* tested samples were designed as a cylinder with φ2.5 mm × 5.6 mm. The printing process parameters for pure Ti were set as follows: laser power (P_L) = 80 W, scanning speed (V_S) = 450 mm/s, hatching space (H_S) = 80 μm and layer thickness (D_S) = 40 μm. For pure Zn, the printing parameters were P_L = 60 W, V_S = 350 mm/s, H_S = 70 μm and D_S = 30 μm. The preparation of the Zn/Ti composites began with Ti printing, followed by remelting of the interface area and Zn printing (Fig. S1b). The remelting parameters for the interface area were the same as those used for printing Zn, and the vertical distribution ratio of Ti to Zn was set at 1:1. Macroscopic images of the built-samples were shown in Fig. S1c.

2.2. Sample characterization

2.2.1. Microstructure characterization

As-built samples were polished with argon ions. Then, the morphology and element distribution of cross-section of the samples were observed using SEM and EDS. An X-ray diffractometer (XRD, Rigaku SmartLab 9 kW, Japan) was used to examine the metal phases with scanning range from 10° to 80° at a scan rate of 2°/min and a step size of 0.02°. Finally, the samples were polished with argon ions and characterized for grain size and texture using electron backscatter diffraction (EBSD, Bruker Dimension Icon, Germany).

2.2.2. Mechanical tests

According to GB/T 7314-2017 and GB/T 228.1–2010, the samples of mechanical tests were fabricated, and both compression and tensile tests were conducted using a universal testing machine (CMT5105, China) at 25 °C. The loading direction for both tensile and compression was set to be parallel to the building direction, and three replicate samples were tested. For the compression test, the displacement rate was set as 0.1 mm/s. For the tensile test, the displacement rate was set as 0.02 mm/s, and the fracture location of the samples was recorded.

2.2.3. Electrical characterization

The interface area of Zn/Ti composites was polished using argon ions. Then, the three-dimensional morphology and potential distribution of the interface area were determined using a kelvin probe force microscope (KPFM) system equipped on an atomic force microscope (AFM). The KPFM measurements were carried out at room temperature by setting the drive routing to the sample, with a scan frequency of 1 Hz. The 3D images of 256 × 256-pixel attribute maps were obtained using NanoScope software.

Additionally, the samples were immersed in a polytetrafluoroethylene (PTFE) chamber filled with a saline solution, with both ends of the chamber sealed with glass fiber filters. The chamber was then connected to a multichannel potentiostat via titanium rods. The open circuit voltage (OCV) of samples within 24 h was measured, and three measurements were conducted to obtain a representative curve result.

2.3. In vitro degradation behavior

2.3.1. Electrochemical tests

The local corrosion behavior of samples was estimated using scanning vibrating electrode technique system (SVET, Applicable Electronics Inc., USA), which could determine the local ionic concentration shift in solution near the sample's surface. And the real-time in situ corrosion current density distribution of samples was recorded in Hanks' Balanced Salt Solution (HBSS, Table S1) for 24 h. The electrochemical tests were conducted with an electrochemical workstation (Autolab, Metrohm, Switzerland) at 37 °C in HBSS. A standard three-electrode system was utilized with the sample as the working electrode, a platinum plate as the counter electrode and a saturated calomel electrode as the reference electrode. The samples of each group were immersed in HBSS for 10 min to stabilize the OCP before the testing. Next, EIS measurements were performed over a frequency range of 10^{-2}–10^5 Hz with a perturbation of 10 mV. A potentiodynamic polarization (PDP) scan was performed at a scan rate of 0.5 mV/s, covering a potential range from −2.6 V to −0.5 V. The corrosion potential (E_{corr}) and corrosion current density (i_{corr}) were analyzed by Tafel extrapolation and linear fit. The OCP tests were carried out with a time period of 3600 s.

2.3.2. Immersion tests

According to ASTM-G31-72, the immersion tests were conducted in HBSS at 37 °C for 28 days, maintaining a solution-to-surface area ratio of 20 mL/cm². The HBSS was refreshed every 3 days. After immersion, the surface and cross-sectional morphology of samples were observed by SEM and EDS, and the corrosion products were identified using XRD. Then, the samples were ultrasonically cleaned with 10 % chromic acid solution (Aladdin, China) for 5 min to remove the corrosion products. The corrosion rate (*CR*) was calculated according to the following formula:

$$CR = \frac{K \times \Delta W}{A \times D \times T}$$

where *CR* was the degradation rate in mm/year, $K = 8.76 \times 10^4$, ΔW was the weight loss of samples in grams, A was the surface area of the sample in cm², D was the density of the sample in g/cm³, and T was the duration of the immersion in hours.

Finally, to determine the concentration of Zn^{2+} released from the samples, the samples were immersed in HBSS for 3, 7, 14, 28 days, and HBSS was not refreshed. At the appointed time points, the concentration of Zn^{2+} in the HBSS was measured by inductively coupled plasma-mass spectrometry (ICP-MS, Agilent 7700, USA).

2.4. In vitro antibacterial activity

2.4.1. Bacterial viability and morphological analysis

Staphylococcus aureus (*S.aureus*, ATCC 25923) and *Escherichia coli* (*E. coli*, ATCC 25922) purchased from Beijing Microbiological Culture Collection Center were used to evaluate the *in vitro* antibacterial performance. Bacteria were cultured in tryptone soy broth (TSB, Solarbio, China), centrifuged, collected, and adjusted to a concentration of 1×10^6 CFU/mL for further use. The sterilized samples were placed in 5 mL of bacterial suspension with a concentration of 1×10^6 CFU/mL, and incubated for 24 h at 37 °C. Then, the bacterial suspension was collected, and serially diluted to spread evenly onto the tryptone soy agar (TSA, Solarbio, China) bacterial culture plates, and incubated at 37 °C for 24 h, to observe the growth viability of the bacteria.

Further, the samples co-cultured with the bacterial suspensions were washed with PBS. The bacteria adhered to the surface of samples were fixed with 4 % paraformaldehyde, then dehydrated by ethanol (30 %, 50 %, 70 %, 80 %, 90 %, 95 %, 100 %, 100 %) gradient dehydration, and dried in a vacuum drying oven. The bacterial morphology was observed using SEM.

2.4.2. Antibiofilm activity

The anti-biofilm effect of each sample group was assessed using crystal violet staining. The samples were placed in 6-well plates and immersed in 2 mL of *S. aureus* and *E. coli* bacterial solutions, each at a concentration of 1×10^6 CFU/mL. After incubating at 37 °C for 72 h, the samples and excess bacterial solutions were removed and gently rinsed twice with PBS buffer. The bacterial biofilms were then fixed with 4 % paraformaldehyde for 15 min, then stained with 0.1 % crystal violet (Beyotime, China) for 15 min at room temperature. Excess stain was washed away, and the bacterial biofilms were photographed. Subsequently, 95 % ethanol was used to dissolve the crystal violet from the biofilms for 10 min, and the absorbance was measured at 570 nm using a

microplate reader after transferring the solutions to a 96-well plate.

2.4.3. Reactive oxygen species (ROS) level evaluation

ROS generated by adhered bacteria on the samples were determined using a bacterial ROS detection kit (BioRab, China). The bacterial suspensions were diluted to 1×10^5 CFU/mL with TSB medium. Next, the samples were placed in 5 mL of bacterial suspension to incubate at 37 °C for 24 h. The samples were transferred to a 12-well plate, and 800 μL of ROS fluorescent probe solution was introduced and reacted at 37 °C in a dark environment for 30 min. The green fluorescent images were captured by a fluorescence microscope (Olympus, Japan).

2.5. In vitro cellular tests

2.5.1. Cell culture and extracts preparation

Mouse osteoblast precursor cells (MC3T3-E1) were purchased from the Cell Bank of the Chinese Academy of Sciences (Shanghai, China). MC3T3-E1 cells were cultured at 37 °C, 5 % CO$_2$ and 95 % humidified atmosphere using α-MEM (Gibco, USA) complete medium, containing 10 % fetal bovine serum (FBS, Gibco, USA) and 1 % penicillin-streptomycin solution (Solarbio, China), and sub-cultured when the cells reached 80 %–90 % confluence. Cells in passages 3–8 were used in this study. The sample extracts were obtained according to ISO 10993-5. All samples were sterilized by Co-60 irradiation, and then immersed in α-MEM complete medium for 24 ± 0.5 h at 37 °C in a cell incubator, with an extraction ratio of 1.25 cm^2/mL. The Zn^{2+} concentrations in the sample extracts were determined by ICP-MS (Agilent 7700, USA). Given the slow degradation rate of Zn-based BMs *in vivo*, and the rapid metabolic exchange of corrosion products, 30 % and 10 % diluted extracts were used for subsequent *in vitro* experiments.

2.5.2. Cell viability and morphological analysis

The Cell Counting Kit-8 (CCK-8, APExBIO, USA) was used to evaluate the cell viability of MC3T3-E1. The cells were seeded into a 96-well plate at a density of 2×10^3/well until they attached to the well bottom. Then, the original medium was replaced with sample extracts to continue the culturing for 1, 3, and 5 days. At specific time points, 10 μL CCK-8 solution was added and incubated at 37 °C for 1 h in the dark. The optical density (OD) value was detected at 450 nm using a microplate reader (Bio-Tek, USA). Finally, cell viability was calculated according to the equation below: Cell viability (%) = [(OD value of experimental group – OD value of blank group)/(OD value of control group – OD value of blank group)] × 100 %. For Live/dead cell staining, MC3T3-E1 cells were co-cultured with 10 % and 30 % extracts. The cells were stained with a Live/Dead cell staining kit (Beyotime, China) and observed by a fluorescence microscope to assess survival and morphology of the cells.

The adhesion morphology and distribution of MC3T3-E1 cells on the surface of samples were observed by SEM. The sterilized samples were co-cultured with MC3T3-E1 cells for 24 h. Then, the samples were washed with PBS, fixed with 4 % paraformaldehyde fixing solution, and gradually dehydrated using a gradient of ethanol at concentrations of 30 %, 50 %, 70 %, 80 %, 90 %, 95 %, 100 %, and 100 %. Finally, the samples were dried in a vacuum drying oven, and the cells on the samples were observed.

2.5.3. In vitro osteogenic differentiation

MC3T3-E1 cells were seeded in a 12-well plate at a density of 2×10^4/mL, and cultured with osteogenic induction extracts, which contained sample extracts, 10 mM β-glycerophosphate (Sigma, USA), 0.1 mM dexamethasone (Solarbio, China) and 0.05 mmol/L vitamin C (Solarbio, China). After 7 days of incubation, cells were lysed using inhibitor-free Western and IP cell lysis buffers (Beyotime, China) and total protein was extracted. The bicinchoninic acid protein assay kit (BCA, Thermo Fisher, USA) was used to determine the total protein content. The ALP detection kit (Beyotime, China) was applied to detect the ALP activity of MC3T3-E1, and the results were expressed in U/mg of

total protein. Moreover, MC3T3-E1 cells were stained using an ALP staining kit to evaluate the ALP expression level. Alizarin Red (Solarbio, China) was used to stain the calcified nodules formed by MC3T3-E1 cells after 28 days of culturing. Then, calcified nodules were dissolved using 10 % of cetylpyridinium chloride (Solarbio, China), and the OD value was measured at 562 nm.

2.5.4. Effect of electrical stimulation on cellular biological functions

In order to verify the effects of the potential difference on cellular biological functions, an electrical signal generation system (ESGS) was designed to simulate the voltage generated by the potential difference of Zn/Ti composites, based on the results of the above electrical characterization. The ESGS consisted of three parts, a stimulation power supply (MS155DS, MAISHENG, China), a platinum sheet for voltage generation, and a cell culture device (Fig. 6a). The ESGS could generate a voltage of 300 mV in the medium via the electrode. The cells co-cultured with 10 % extracts of Zn/Ti composites were exposed to the continuous stimulation of voltage, and the cell viability and osteogenic differentiation were observed by CCK-8, Live/Dead cell staining and ALP tests. According to the external intervention conditions, the following three groups were designed: (*i*) Blank (No Zn^{2+} and electrical stimulation); (*ii*) Electric (E)-active (Only electrical stimulation without Zn^{2+} intervention); (*iii*) Zn&E-active (Electrical stimulation and Zn^{2+} co-intervention).

2.5.5. RNA sequencing

After 7 days of continuous culture of MC3T3-E1 cells by ESGS and extracts. The total RNA from cells was extracted using an Eastep® Super Total RNA Extraction Kit (Promega, USA). RNA sequencing was performed by Majorbio (Shanghai, China) to analyze the expression profiles of mRNAs. The TruSeq Stranded mRNA LTSample Prep Kit (Illumina, USA) was used to build the transcriptome sequencing library. The NovaSeq X plus platform (Illumina, USA) was applied for transcription sequencing. The differentially expressed genes (DEGs) were regarded as those with |log2(Fold Change)| > 1 and q-value <0.05. A volcano plot was adopted to exhibit the DEGs, and the expression levels of DEGs were demonstrated by clustering heatmap. Subsequently, functional enrichment analysis, including GO and KEGG, were performed to identify which DEGs were significantly enriched in GO terms and metabolic pathways, utilizing the Goatools and Python scipy software.

2.6. In vivo implantation

2.6.1. Surgical process

The samples (φ2.5 mm × 5.6 mm) were used for *in vivo* implantation. All animal operations were approved by the Animal Ethics Committee of the Beijing Keyu Animal Breeding Center (KY20230426002). 24 male rats weighing 200–250 g were anesthetized with an intraperitoneal injection of ketamine (10 mg/kg, Dr. Ehrenstorfer GmbH, Germany) and 2 % xylazine (10 mg/kg, Fluorochem, UK). A longitudinal incision was made lateral to the patellar ligament to expose the lateral femoral condyle. A mono-cortical perforating bone defect model for the rat lateral femoral condyle was established via drilling with a 2.4 mm drill bit. Samples were implanted into the defect, with the Zn part of the Zn/Ti composites facing inward. Then, the surgery site was sutured layer by layer. The rats were euthanized at 4, 8, and 12 weeks post-implantation to collect femurs.

2.6.2. Micro-computed tomography (Micro-CT) analysis

The collected rat femurs were fixed with 4 % paraformaldehyde solution. The fixed femurs were scanned by Micro-CT (Zeiss Xradia 520 Versa, Germany, 120 kV, 66.7 μA) and imaged using the 3D image processing software CTvox 3.0 (Bruker, Germany). The region of interest (ROI) was defined as a cylindrical area of φ3 mm × 6 mm, with the samples located in the centre of the ROI. The bone volume fraction (BV/TV), trabecular numbers (Tb.N), trabecular thickness (Tb.Th), and

trabecular separation (Tb.Sp) in the ROI were analyzed quantitatively to evaluate the bone formation.

2.6.3. Histological analysis

The collected femurs were first dehydrated with ethanol, subsequently cleaned with dimethylbenzene, and ultimately embedded in methyl methacrylate. Three to four 200 μm-thick sections were cut along the vertical axis of the samples, ground and polished to 100 μm-thick, stained with methylene blue-basic magenta, and imaged under a microscope. The remaining tissue blocks at 12 weeks were analyzed using SEM and EDS. Additionally, organ specimens including the heart, liver, spleen, lung, and kidney from SD rats were stained with hematoxylin-eosin (H&E) 12 weeks after implantation.

2.7. Statistical analysis

All quantitative data were expressed as Mean $\pm$ standard deviation (SD). The SPSS 23.0 statistical software (IBM, USA) was used to assess the statistical significance of the data by the one-way analysis of variance (ANOVA). $*p < 0.05$ or $**p < 0.01$ were considered statistically significant.

3. Results

3.1. Sample characterisation

3.1.1. Microstructure

The microstructural morphology and elemental distribution of the cross-sections of the samples (Fig. 1a) show that no obvious cracks were observed in the interfacial bonding region of the Zn/Ti composites, indicating strong bonding between Zn and Ti. Notably, a small amount of Ti was found in the Zn region close to the interface, which may be attributed to the disturbance of molten pool during the printing of Zn, where the liquid Ti were sputtered into the Zn region due to the strong laser-melt interaction. To further clarify the microstructure of the samples, EBSD results were illustrated in Fig. 1b. The Ti samples showed a uniformly distributed plate-like and blocky α phase with grain sizes of about 7.3 μm. Obvious columnar crystals were observed in the Zn samples, with a grain size of about 25.7 μm. By contrast, the Ti region of the Zn/Ti samples also showed a uniformly distributed plate-like and blocky α phase organization, while the Zn region had a transition from equiaxed crystals in the interfacial region to columnar crystals away from the interfacial region. In addition, significant grain refinement was
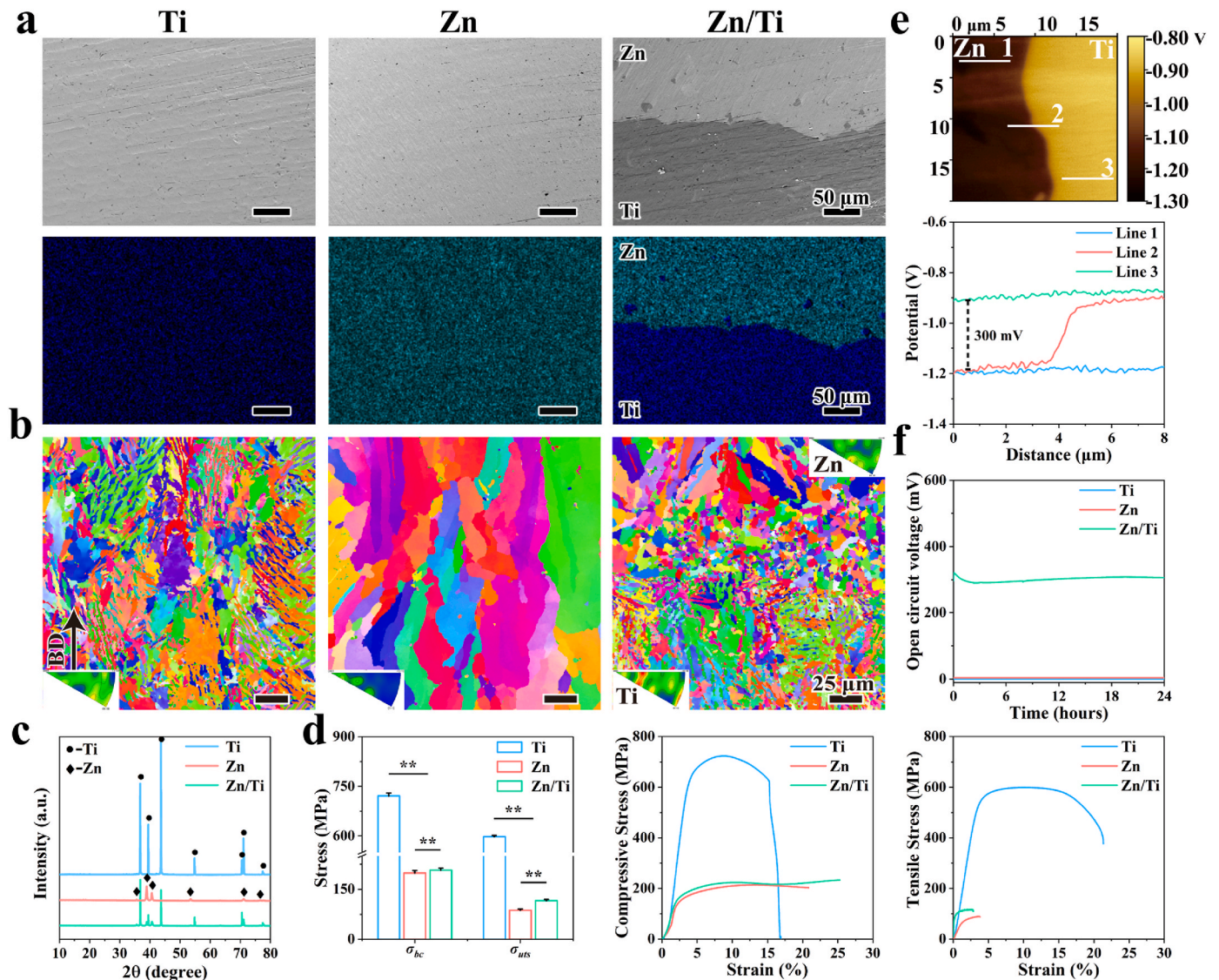

Fig. 1. (a) SEM and EDS images of the cross section of different samples; (b) EBSD maps of the cross section; (c) XRD patterns; (d) Mechanical properties of different samples; (e) The potential distribution of Zn/Ti samples, and (f) open circuit potential of the samples in saline.

observed in the Zn/Ti samples, with the average grain sizes in the Ti and Zn regions of about 6.0 μm and 6.4 μm, respectively. The grain refinement in the Zn region was more pronounced, and the grains in the interfacial region were much thinner than those in the far from interfacial region. The XRD patterns of the samples were shown in Fig. 1c, with the Zn/Ti composites containing the diffraction peaks of Ti and Zn. No secondary phases were observed in the XRD patterns of Zn/Ti composites.

3.1.2. Mechanical properties

Fig. 1d demonstrated the mechanical properties of the samples. Among them, Ti exhibited the highest compressive strength (σ_{bc}) of 726.66 ± 3.5 MPa. The σ_{bc} of the Zn and Zn/Ti composites was recorded at 200 ± 6.5 MPa and 210 ± 5.3 MPa. The ultimate tensile strength (σ_{uts}) of Ti, Zn and Zn/Ti composites were 599.1 ± 3.5 MPa, 89.6 ± 3.1 MPa, and 117.1 ± 2.0 MPa, respectively. Moreover, the tensile fracture of the Zn/Ti composites occurred in the Zn region (Fig. S2), which indicated a strong interfacial bond between Zn and Ti, where the interfacial bonding strength exceeded the σ_{uts} of Zn.

3.1.3. Potential distribution and potential difference

The potential distribution and potential difference of Zn/Ti composites were demonstrated in Fig. 1e. Uniform potential distributions were observed in the regions of Zn and Ti, with the relative potential fluctuating around −1.2 V in the Zn region (Line 1), and around −0.9 V in the Ti region (Line 3). A steep potential difference of about 300 mV was observed at the interfacial region between Zn and Ti (Line 2). The measured relative potential was determined as the difference between the Kelvin probe potential and the samples. Therefore, in the Zn/Ti composites, the potential of Zn was found to be 300 mV higher than that of Ti. Furthermore, to verify the generation electrical stimulation of the samples in a physiological environment, the open circuit voltage (OCV) of the samples was measured when the samples were rested in saline. As shown in Fig. 1f, no voltage output was observed in the pure Zn and Ti groups, whereas the Zn/Ti composites stably outputted a voltage of about 300 mV over the 24 h test period.

3.2. In vitro degradation behavior

The real-time in situ corrosion current density distribution of scaffolds was recorded using SVET, as shown in Fig. 2a. After 24 h of immersion, the current densities of Zn and the Ti region of Zn/Ti were low and stable, whereas the current densities in the Zn region of Zn/Ti exhibited were higher, indicating more severe degradation.
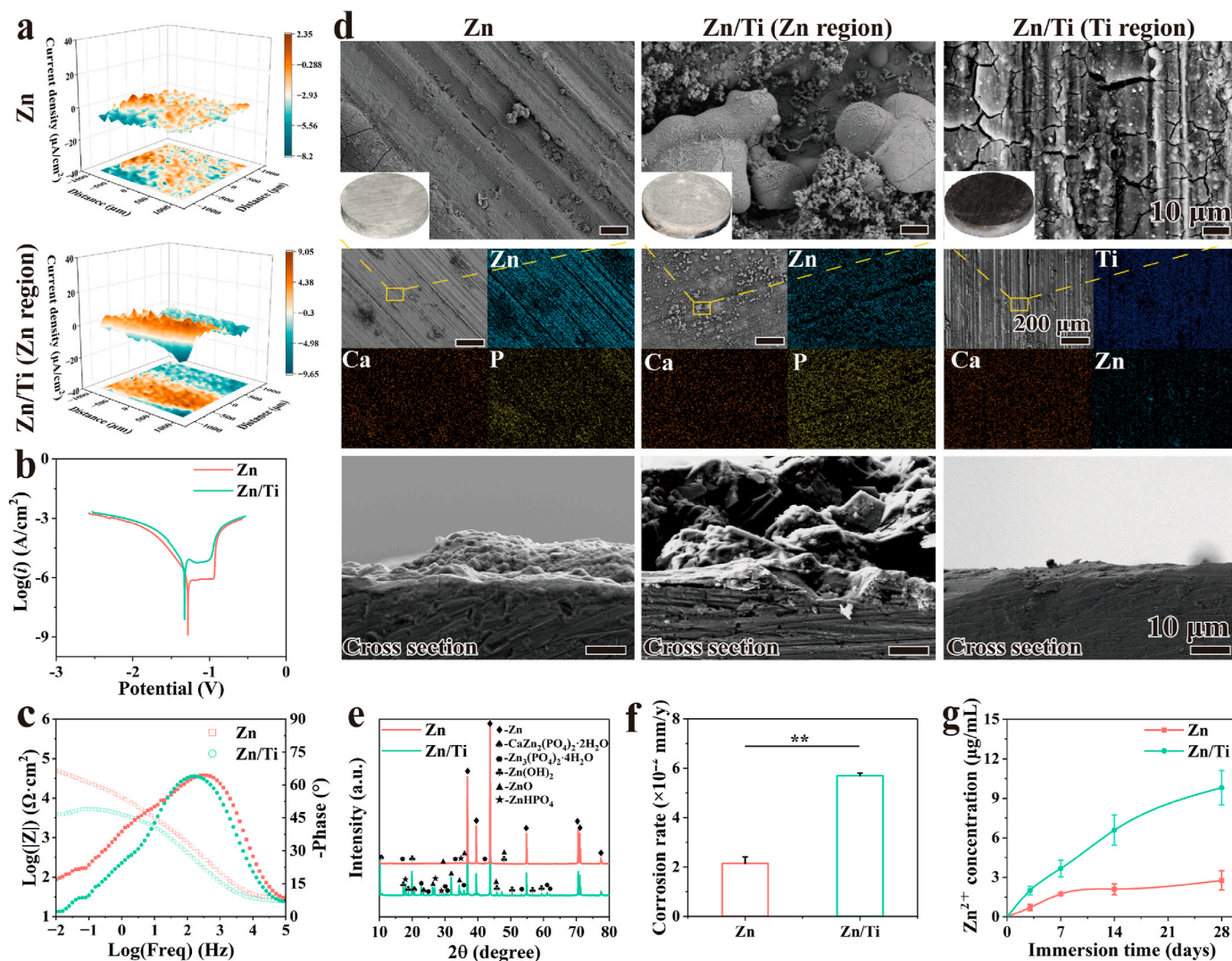

Fig. 2. *In vitro* degradation behavior of Zn and Zn/Ti composites: (a) 3D SVET maps, (b) PDP curves, (c) Bode plots, (d) Overview pictures, SEM and EDS scan images of the sample surface and cross section after 28 days of immersion, (e) XRD patterns of degraded Zn and Zn/Ti samples after 28 days, (f) Corrosion rates, and (g) Zn^{2+} concentration in HBSS.

Electrochemical tests were performed to evaluate the early degradation behavior of Zn and Zn/Ti samples. PDP curves were shown in Fig. 2b, and the data calculated by Tafel fitting were provided in Table S2. The Zn/Ti composites showed a lower OCP value of -0.975 V$_{SCE}$ compared to -0.931 V$_{SCE}$ for pure Zn, indicating lower corrosion resistance. Moreover, the corrosion potential (E_{corr}) and corrosion current density (I_{corr}) value of pure Zn were -1.284 V$_{SCE}$ and 1.217×10^{-6} A/cm^2 respectively. Whereas, the Zn/Ti composites displayed a lower E_{corr} of -1.326 V$_{SCE}$ and a higher I_{corr} value of 5.044×10^{-5} A/cm^2, indicating a higher degradation rate. The Bode plots (Fig. 2c) presented the impedance of Zn sample is one order of magnitude larger than that of Zn/Ti, indicating a better corrosion resistance. Both samples showed a declined trend of impedance over time. The Zn/Ti sample exhibited one time constant in the medium to highfrequency zone (10^1–10^5 Hz). In pure Zn, the time constant occupied a wider frequency zone.

The long-term degradation behavior of the samples was further assessed through *in vitro* immersion tests over a 28-day cycle. As shown in Fig. 2d, more white corrosion products were observed in the Zn region of the Zn/Ti samples compared to pure Zn. EDS results revealed a clear enrichment of Zn, Ca, and P elements at the surface of samples, implying the presence of Zn oxides or hydroxides, calciate and phosphates in corrosion products. The XRD results (Fig. 2e) of the degraded samples also confirmed the presence of Zn(OH)$_2$, ZnO, Zn$_3$(PO$_4$)$_2$·4H$_2$O, etc. Moreover, the intensity of the diffraction peaks for the corrosion products in the Zn region of the Zn/Ti samples was significantly stronger than that of the pure Zn. Notably, a small amount of Zn corrosion products was also observed in the Ti region of the Zn/Ti composites, which was attributed to the co-deposition of Zn^{2+} released during Zn degradation with Ca and P elements in HBSS.

The amount of corrosion products was closely related to the degradation rate of Zn. Typically, more corrosion products representing more drastic degradation behavior. After immersion, the corrosion rates of the samples were shown in Fig. 2f. The *in vitro* corrosion rate of pure Zn was about 0.021 mm/y, while the corrosion rate of the Zn/Ti samples was accelerated to 2.7 times, and reached about 0.056 mm/year. Furthermore, the concentration of Zn^{2+} released by the samples in HBSS was monitored. As shown in Fig. 2g, the release of Zn^{2+} in all samples was rapid in the initial 7 days. The Zn^{2+} release from pure Zn gradually stabilized after 7 days, which could be attributed to the formation of corrosion products on the sample surface, thereby hindering the contact of the corrosive medium with the Zn matrix. However, the concentration of released Zn^{2+} from the Zn/Ti composites continued to increase, despite the presence of more corrosion products on their surface. Moreover, the concentration of released Zn^{2+} from the Zn/Ti samples was consistently much higher than from pure Zn. These results suggested that Zn/Ti composites had an accelerated degradation compared to pure Zn. The results of immersion tests were consistent with electrochemical results.

3.3. In vitro antibacterial performance

The spread plate method was used to evaluate the antibacterial performance of the samples. The pure Ti samples showed no antibacterial performance due to their biological inertness. In contrast, both pure Zn and Zn/Ti samples significantly inhibited the proliferation of *S. aureus* and *E. coli*. The antibacterial effect of Zn/Ti composites was significantly higher than that of pure Zn (Fig. 3a–c). To investigate the effect of different samples on the biofilm-forming ability of *S. aureus* and *E. coli*, crystal violet staining was employed. After 72 h of co-culture with the various samples, a clear color gradient was observed (Fig. 3b). The Ti and control groups formed biofilms comparable in intensity, while the Zn group biofilms appeared somewhat lighter, and the Zn/Ti group nearly completely inhibited biofilm formation. The semi-quantitative results of crystal violet also confirmed this trend, with the lowest OD value observed in the Zn/Ti group (Fig. 3d).

In addition, the adhesion and growth status of bacteria on the sample surfaces were observed (Fig. 3e). A large number of bacteria adhered to the surface of pure Ti. In comparison, the limited bacterial adhesion was observed on pure Zn, and some bacteria exhibited shrunken and ruptured morphology. The least bacterial adhesion was observed in the Zn region of Zn/Ti samples. Also, the limited bacterial adhesion and crumpled bacterial morphology were found within the Ti region of the Zn/Ti samples.

The expression level of bacterial ROS was a critical indicator of the degree of bacterial response to external stimulation. The results of ROS staining of bacteria co-cultured with the samples were shown in Fig. 3f. No obvious green fluorescence, representing ROS expression, was found on the surface of pure Ti. In contrast, significant fluorescent signals were found in both the pure Zn and the Ti region of Zn/Ti samples. The strongest fluorescent signals were observed in the Zn region of Zn/Ti samples. These results mentioned above indicated that the antibacterial performance of Zn/Ti composites was significantly enhanced compared to pure Zn.

3.4. In vitro cytocompatibility and osteogenic activity

3.4.1. Cell viability and morphological analysis

The proliferative viability of the cells co-cultured with sample extracts was evaluated by CCK-8 method. As shown in Fig. 4a, the concentration of Zn^{2+} within the pure Zn extracts was about 28.83 ± 2.54 μg/mL. The Zn^{2+} concentration of the Zn/Ti extracts increased to 54.29 ± 8.86 μg/mL. Fig. 4b demonstrated the CCK-8 results, pure Ti exhibited a good cytocompatibility. And the pure Zn extracts exhibited significant cytotoxicity at a concentration of 50 %, whereas the cell proliferation was promoted at concentrations of 30 % and 10 %, suggesting good cytocompatibility at low concentrations of Zn^{2+}. In contrast, the Zn/Ti extracts showed a significant cytotoxicity at both 50 % and 30 % concentrations. However, the cell viability was improved, when the Zn/Ti extracts were diluted to 10 % concentration, which reached about 120 % at 5 days.

The results of live/dead cell staining were shown in Fig. 4c. A reduced number of live cells and poor cell morphology were observed in the 30 % extracts of Zn/Ti samples, suggesting apparent cytotoxicity. Conversely, cells cultured in 10 % extracts of Zn/Ti samples exhibited normal stretching morphology with pike shapes, irregular triangles and visible pseudopods. No abnormal cell death was observed in the 30 % and 10 % pure Zn extracts. Fig. 4d demonstrated the adhesion morphology of MC3T3-E1 cells on the sample surfaces. The cells on the pure Ti surfaces displayed normal stretching morphology. In contrast, the cells on pure Zn surfaces appeared spherical, implying significant contact inhibition. Cells adhering to the Zn region of Zn/Ti samples showed a slightly improved spreading morphology compared to those on pure Zn, and the stretching of pseudopods was observed on the cells within the Ti region of Zn/Ti samples.

3.4.2. In vitro osteogenic differentiation

The effect of the samples on osteogenic differentiation of MC3T3-E1 cells was evaluated by ALP and ARS tests. As shown in Fig. 5a, both the pure Ti group and the negative control group demonstrated similar levels of osteogenic induction activity. The cells co-cultured with 30 % Zn/Ti extracts died significantly, while 30 % pure Zn extracts showed enhanced ALP activity and extracellular matrix mineralization. In the 10 % extracts, the pure Zn group did not exhibit a promoting effect on osteogenic differentiation, due to the too low Zn^{2+} concentration. However, the 10 % concentration extracts of Zn/Ti samples significantly enhanced osteogenic differentiation, compared to the other samples. The quantitative and semi-quantitative analysis of ALP activity and mineralization levels confirmed these observations (Fig. 5b and c). These results indicated that appropriate concentrations of Zn^{2+} significantly improved osteogenic differentiation of MC3T3-E1 cells.
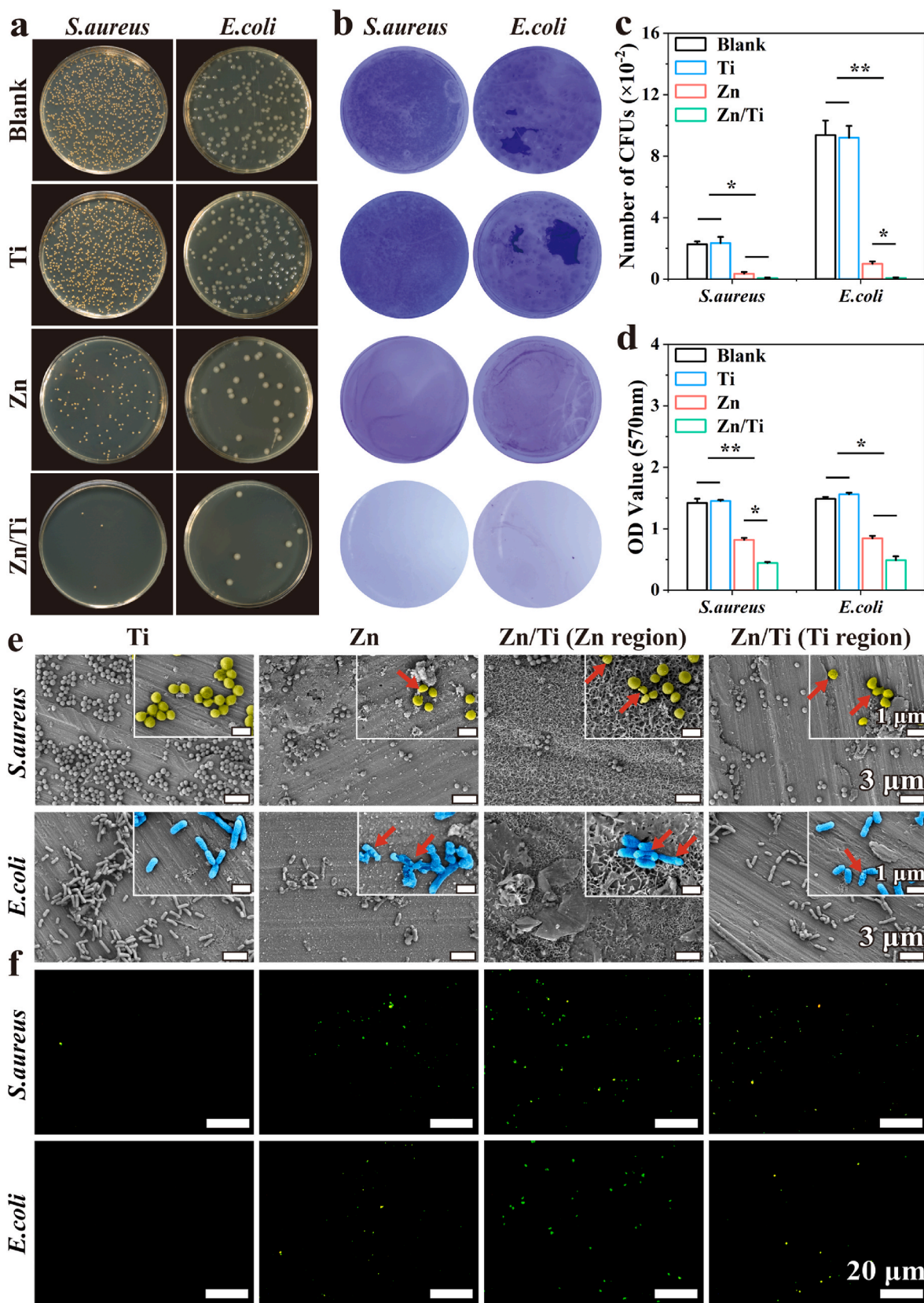
Fig. 3. *In vitro* antibacterial performance of the samples: (a) Images of *S. aureus* and *E. coli* bacterial colonies after co-cultured with samples, (b) Effect of samples on biofilm formation of *S. aureus* and *E. coli*, (c) Counts of *S. aureus* and *E. coli* bacterial colonies after co-cultured with samples, (d) Semi-quantitative analysis after dissolution by crystalline violet staining, (e) SEM images of *S. aureus* and *E. coli* on the surface of samples, and (f) Fluorescence images of *S. aureus* and *E. coli* bacterial ROS expression levels after co-cultured with samples.
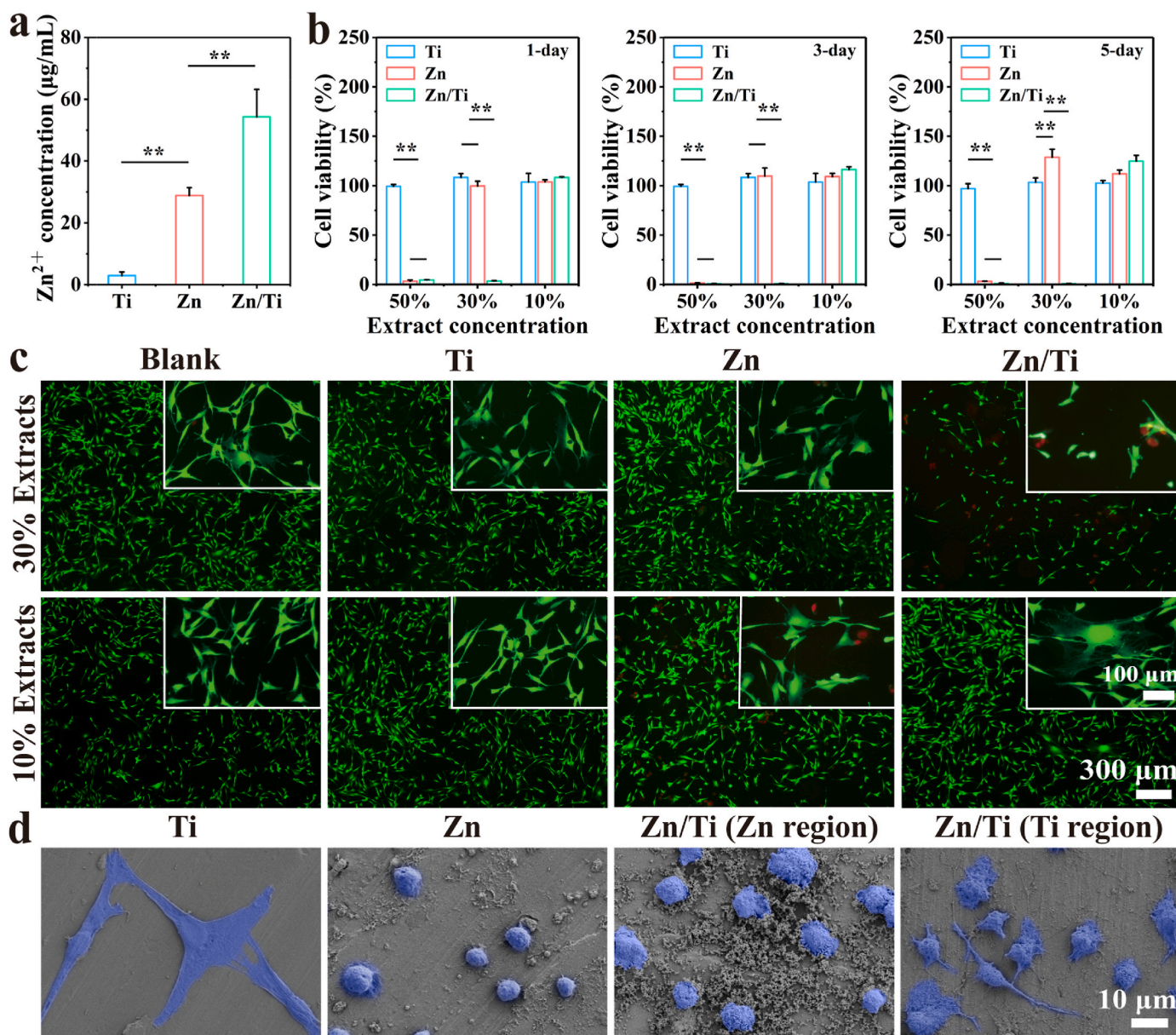
Fig. 4. *In vitro* cytocompatibility of the samples: (a) Zn^{2+} concentration in extracts, (b) Cell viability of MC3T3-E1 co-cultured with different sample extracts, (c) Live/Dead staining images of MC3T3-E1 cells, and (d) The morphology of MC3T3-E1 cells on the surface of samples after co-culture.

3.4.3. Effects of electrical stimulation on cellular biological functions

Following stimulation of MC3T3-E1 cells with a 300 mV voltage signal from the ESGS device (Fig. 6a), the results of the cell viability test were shown in Fig. 6b. Cells in both E-active and Zn&E active groups exhibited an improved proliferation, with the cell viability reaching approximately 112 % after 3 days. After 5 days of culture, the Zn&E-active group demonstrated the highest cell viability at around 126 %. Live/dead cell staining results (Fig. 6c) also showed a similar trend, and the highest number of live cells was observed in the Zn&E-active group. Further, the test results of the ALP activity were shown in Fig. 6d and e. ALP activity was significantly up-regulated in the E-active group at a voltage of 300 mV, and the highest ALP activity was detected in the Zn&E-active group. These results indicated that the synergistic effect of 300 mV voltage signal with Zn^{2+} could enhance the biological functions of MC3T3-E1 cells, including proliferation and differentiation.

3.4.4. Investigation of osteogenic mechanism of Zn/Ti composites

To explore the biomolecular mechanisms underlying osteogenic differentiation induced by Zn/Ti composites, transcriptomic analysis was performed. The volcano plot (Fig. 7a) revealed 152 up-regulated and 367 down-regulated genes in the E-active group, whereas the Zn&E-active group exhibited 356 up-regulated and 262 down-regulated genes. Additionally, comparison between the Zn&E-active and E-active groups showed 377 up-regulated and 250 down-regulated genes. These results indicated that gene expression in MC3T3-E1 cells was significantly influenced by the synergistic action of Zn^{2+} and voltage signals. The heatmap results were shown in Fig. 7b. Compared to the blank group, The expression of osteogenesis-related genes including Col2α1, Sparc, and Ror2, was significantly up-regulated in the E-active group. In the Zn&E-active group, a higher expression of osteogenesis-related genes (Col2α1, Bglap, Bglap2, Spp1, Lgr6) was also observed. Moreover, significant up-regulation of metallothionein genes (*Mt1*, *Mt2*) expression was observed in the Zn&E-active group.

The results of GO enrichment analysis (Fig. 7c) further indicated that the differential genes of Zn&E-active group enriched in cell adhesion, biomineral tissue development, bone mineralization, and osteoblast
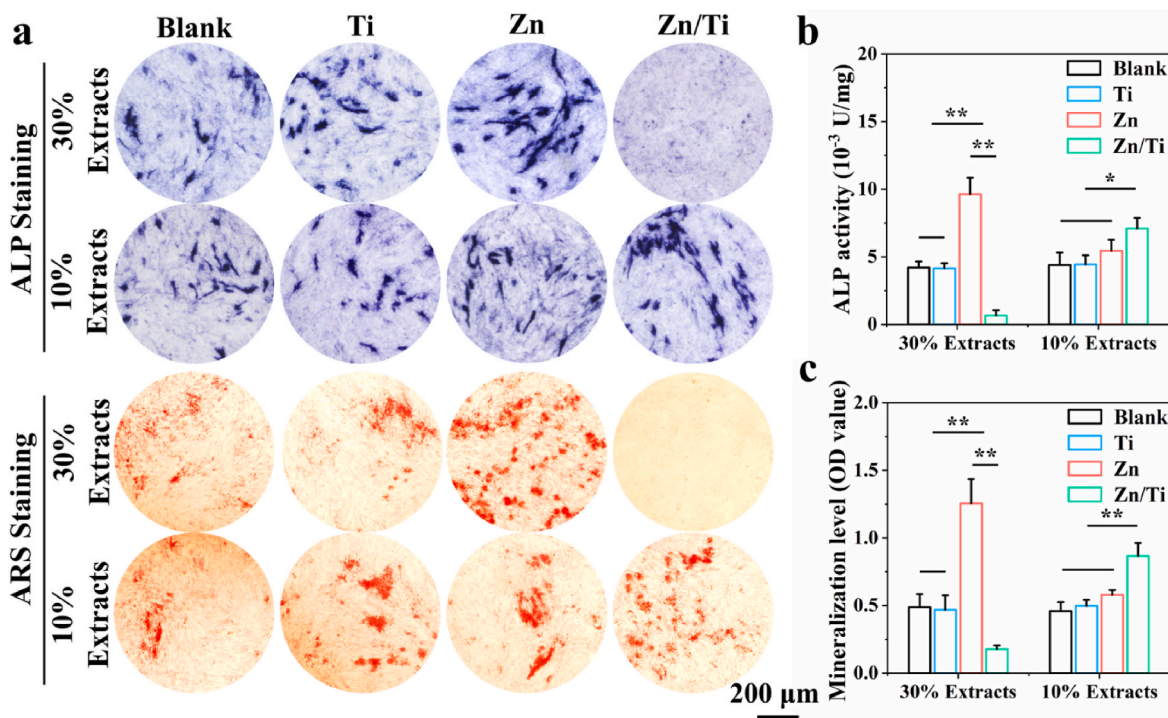
Fig. 5. *In vitro* osteogenic differentiation: (a) ALP and ARS staining, (b, c) Quantitative and semi-quantitative analysis of ALP activity and mineralization levels.
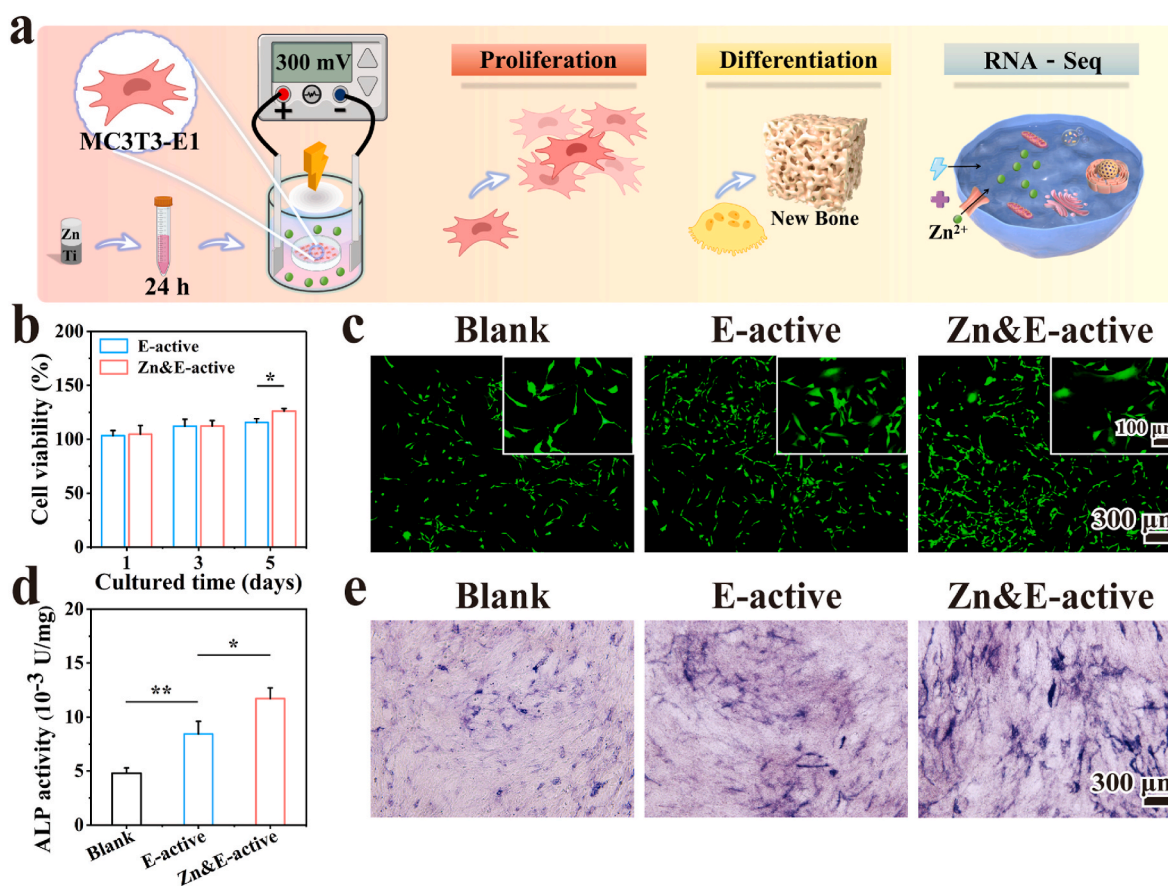

Fig. 6. The effect of voltage signal on the biological function of MC3T3-E1 cells: (a) Schematic representation of the biological function test by ESGS applying voltage signal to the cells, (b, c) Results of the cell viability test, (d, e) Quantitative and qualitative analysis of ALP expression.
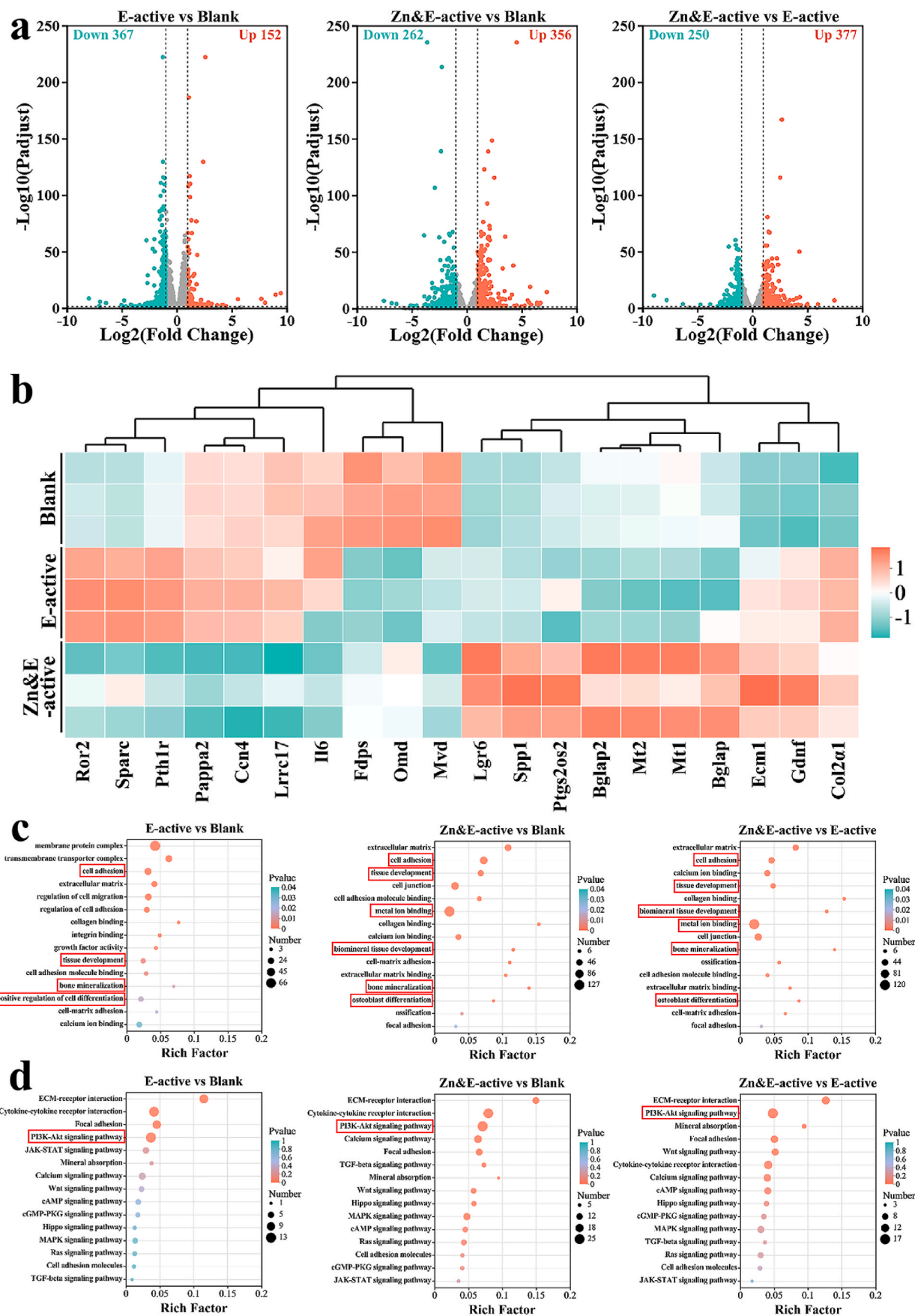
Fig. 7. (a) Volcano maps of DEGs enrichment, (b) Heatmap of DEGs, (c) Significantly enriched GO terms, and (d) Significantly enriched KEGG pathways.

differentiation. A significant increase in genes related to metal ion binding was observed. For the E-active group, the functions of differential genes also enriched in cell adhesion, tissue development and bone mineralization. Next, KEGG enrichment analysis (Fig. 7d) was conducted to explore potential signaling pathways. Significant enrichment of ECM-receptor interaction and PI3K-Akt signaling pathway related to osteogenic differentiation was observed in both the Zn&E-active and E-active groups. These findings explained the superior *in vitro* osteogenic characteristics of Zn/Ti composites.

3.5. In vivo implantation

3.5.1. Micro-CT analysis

As illustrated in Fig. 8a, a small quantity of new bone was observed around all samples at week 4 postoperatively. The amount of new bone gradually increased over time, and at week 8, significantly more new bone was observed around the Ti and Zn/Ti groups compared to the pure Zn. At week 12, the Zn/Ti group showed the most bone formation compared to both pure Ti and pure Zn groups. Notably, within Zn/Ti samples, more new bone was observed in the Ti region, while only a small amount of new bone was present in the Zn region. This may be attributed to the rapid degradation of Zn, resulting in the accumulation of a large amount of degradation products in the Zn region, hindering

direct osseointegration of new bone with the sample. For the Ti region, the distant diffusion of Zn^{2+} and the effect of electrical stimulation may have enhanced the osteogenic activity. Quantitative analyses of osteogenesis-related indicators further confirmed the enhanced osteogenic ability of Zn/Ti samples, since the higher BV/TV, Tb. Th and Tb. N were observed (Fig. 8b).

3.5.2. Histological evaluation

Hard tissue sections were shown in Fig. 9a, where red areas surrounding the implants indicate regenerated bone. The sectioning results revealed significantly more bone formation around the pure Ti and Zn/Ti samples compared to pure Zn (Fig. 9a and b). The direct osseointegration of new bone with the samples was also observed in the pure Ti and the Ti region of the Zn/Ti samples. Additionally, small amounts of dark brown degradation products were observed around the pure Zn samples. By contrast, the Zn region of the Zn/Ti samples exhibited significantly greater accumulation of degradation products. A significant new bone formation was observed around these degradation products, along with direct contact between the new bone and the degradation products. These results indicated that Zn/Ti samples have enhanced osteogenic activity and accelerated degradation behavior compared to pure Zn. The H&E staining results for rat vital organs, including heart, liver, spleen, lung, and kidney sections, were presented
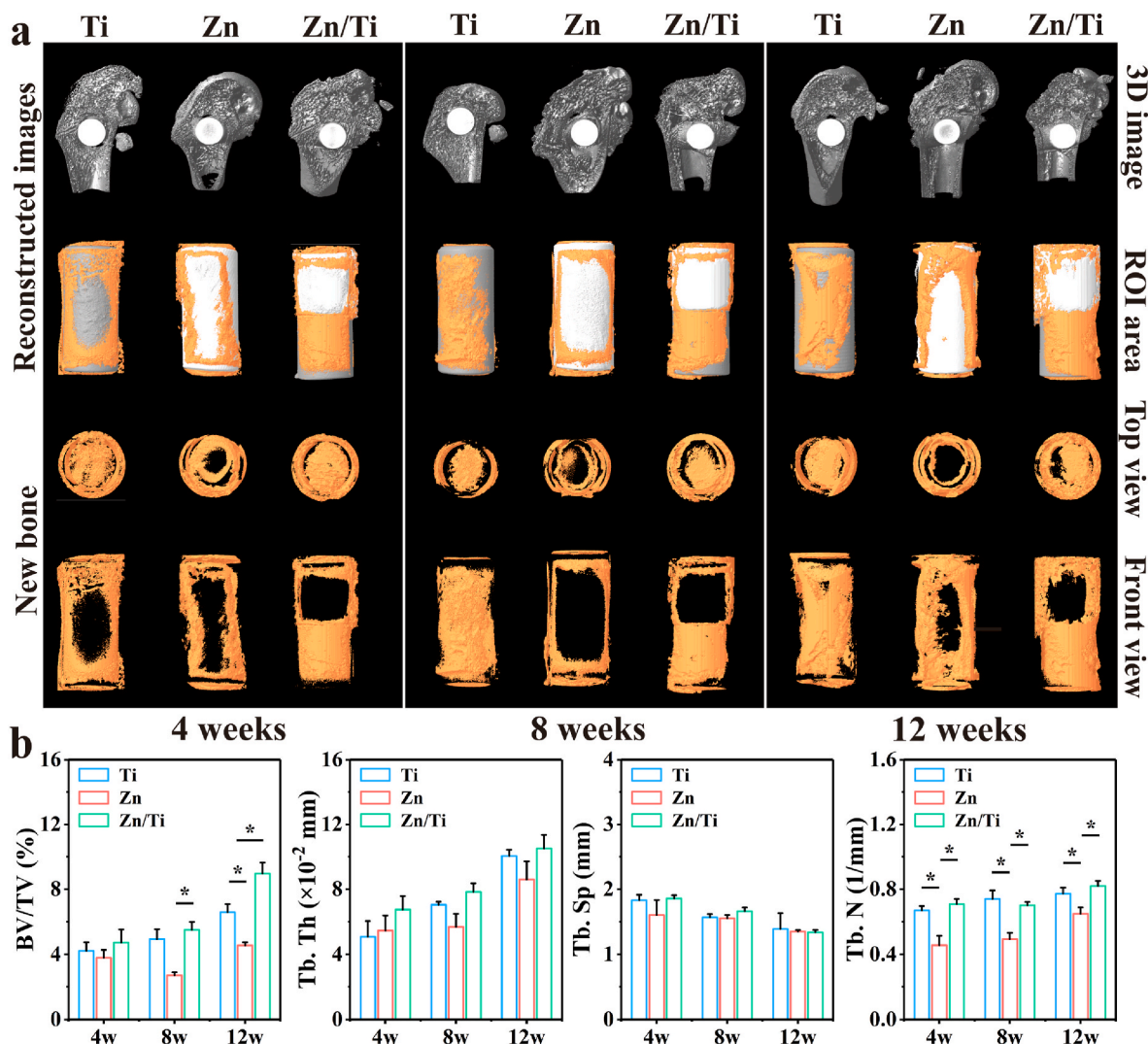

Fig. 8. (a) Micro-CT images at 4, 8, and 12 weeks of *in vivo* implantation including new bone and implants images, (b) Quantitative analyses of osteogenesis-related indicators (BV/TV, Tb. N, Tb. Th, and Tb. Sp).
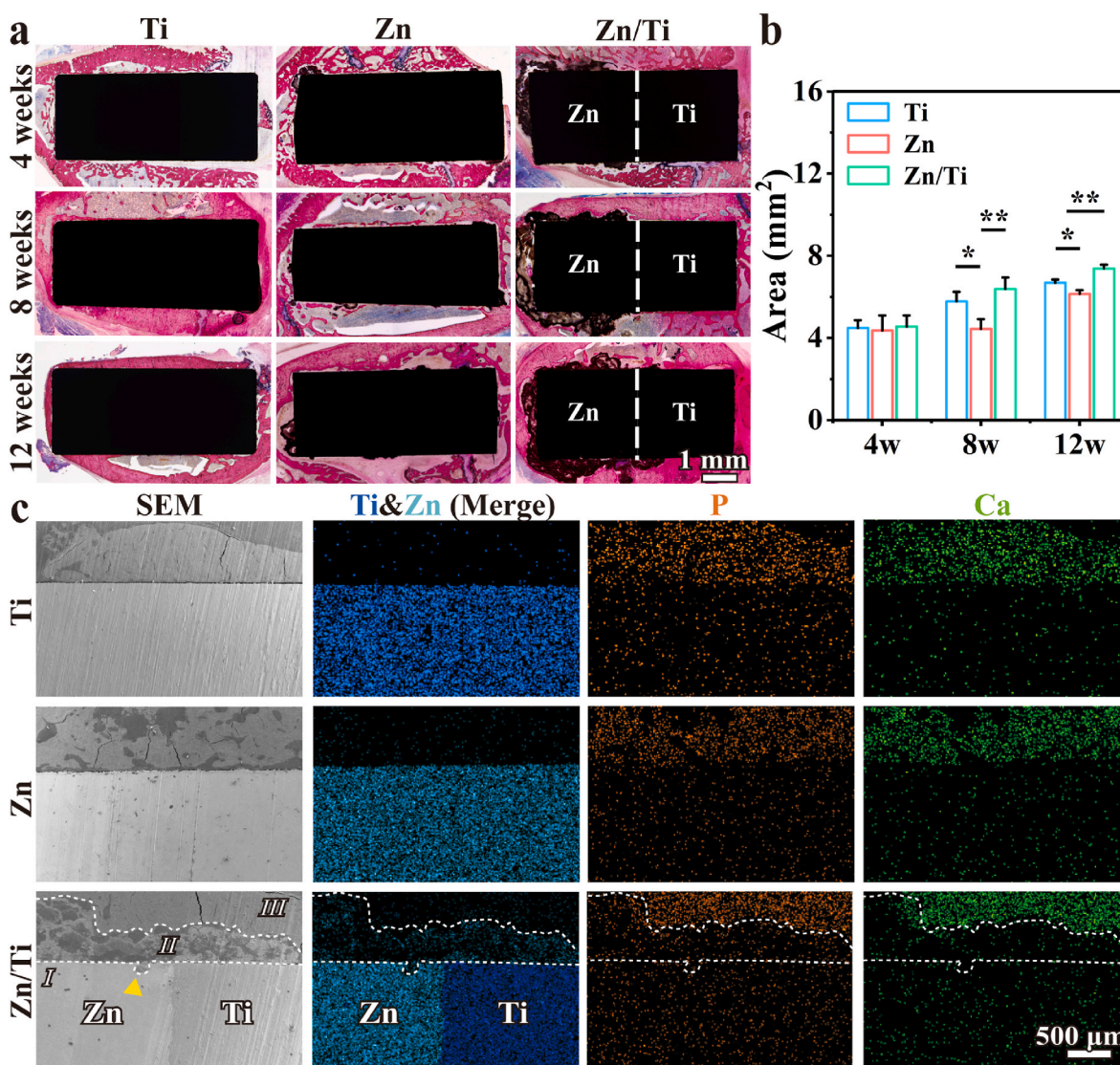
Fig. 9. (a) Full-view images of hard-tissue slices of the samples implanted *in vivo* at 4, 8, and 12 weeks, (b) New bone tissue area analysis, and (c) Cross-sectional SEM images and corresponding EDS mapping results at 12 weeks after implantation.

in Fig. S3. No abnormalities or pathological morphologies were observed in any of the tissue sections, indicating normal vital organ function in the experimental animals and confirming the good *in vivo* biosafety of all samples.

To further determine the *in vivo* degradation behavior and osseointegration ability of the samples, femurs 12 weeks after implantation of the samples were observed by SEM and EDS. As shown in Fig. 9c, Ti was in close contact with the surrounding bone tissues, indicating excellent osseointegration. For the pure Zn, new bone around the samples was also observed. However, insufficient osseointegration was observed in pure Zn group, and only a small amount of degradation products were observed around the samples due to slower *in vivo* degradation. For the Zn/Ti samples, three distinct regions were identified based on the SEM and EDS results: Region *I*, representing the metal implant, showed high intensity signals of the elements Zn and Ti; Region *II*, displaying diffusion of small amounts of the elements Zn, Ca and P, indicated the presence of degradation products; Region *III*, enriched in Ca and P elements, corresponded to the areas of new bone. The extensive degradation products in Region *II*, suggested that Zn/Ti samples have a much higher *in vivo* degradation rate than pure Zn. The accelerated degradation of the Zn/Ti samples was further confirmed by the obvious corrosion pit (marked by the yellow arrow) found in Region *I*. Moreover, no

obvious gaps were found between Region *II* and *III*, suggesting direct contact between the new bone and the degradation products of Zn. These observations were consistent with the trend of the hard histological section results.

4. Discussion

4.1. Microstructure, mechanical properties and electrical characterization

For the metal bone implants fabricated via MMAM technology, high quality of as-built samples is the prerequisite for reliable properties, since the printed process involved the melting and bonding of discrete powders across numerous tracks and layers [32,40]. In this study, no cracks were observed at the Zn/Ti interfacial region, indicating satisfactory fusion quality (Fig. 1a). Moreover, grain refinement and columnar-to-equiaxed transition of Zn grains were found in the interfacial region of Zn/Ti samples (Fig. 1b). This is likely due to the mixing of high-melting point Ti powders, which can suppress the epitaxial grain growth of Zn, and the incompletely melted Ti particles can act as nuclei agent for Zn grains, leading to more equiaxed grains. In the region away from the interface, columnar grains of Zn with large sizes were found due to the epitaxial grain growth. Refined grains have been shown to

enhance the mechanical properties of the metal matrix [41]. However, in Zn/Ti composites, microstructural alterations were confined primarily to the interfacial region. Despite this localized improvement leading to a strong interfacial bond (Fig. S2), the overall mechanical properties of the composites failed to exhibit significant enhancement (Fig. 1d). Notably, the designs in this study did not consider the clinically relevant structural design of porous scaffolds. MMAM technology enables the region-specific distribution of dissimilar metals through structural design [32]. Meanwhile, parameters of the porous structure, including porosity, pore size and strut diameter, can be customized using L-PBF technology, allowing the scaffolds to match the mechanical properties of bone [17]. In future clinical applications, Ti can be deployed in the primary load-bearing anatomical positions, due to its excellent mechanical properties, while Zn can be utilized in the secondary load-bearing or non-load-bearing regions. Furthermore, customized parameters of the porous structure can be applied to macroscopically integrated Zn-based composites, to further modulate their mechanical properties in accordance with the distinct characteristics of dissimilar metals, achieving functionally partitioned applications and overcoming the insufficient mechanical properties of Zn-based BMs.

The contact of dissimilar metals may result in electron transfer due to differences in electronic structure and electrochemical properties, which, in turn, leads to the generation of potential differences [42]. As shown in Fig. 1e, a pronounced potential difference of approximately 300 mV was observed between the Zn and Ti regions of Zn/Ti composites. This potential difference was the primary factor causing the galvanic coupling corrosion of Zn/Ti composites, mediated by body fluids [43]. As reported, the corrosion tendency increased with the potential difference during galvanic coupling corrosion [44]. When the potential difference exceeded 250 mV, the resulting galvanic coupling corrosion was found to be more severe. Consequently, the accelerated degradation behavior of Zn/Ti composites can be predicted, given the occurrence of galvanic coupling corrosion. Furthermore, the potential difference enabled the Zn/Ti composites to generate a stable voltage of approximately 300 mV in physiological saline (Fig. 1f), which indicated that the composites can continuously output a voltage signal to the surrounding tissues *in vivo*. The voltage signal generated by the construction of gradient potentials may play a significant role in regulating bone remodeling, which is similar to piezoelectric materials [31]. Studies have shown that the application of mechanical stress could result in deformation of the crystal structure in the piezoelectric materials, which, in turn, caused a separation of positive and negative charges, thereby generating a potential difference and outputting a voltage signal [45]. This voltage signal can promote the biological functions of osteoblasts, including proliferation and differentiation [46]. Nevertheless, the functional failure of piezoelectric materials under long-term cyclic loading, as well as insufficient mechanical properties, has caused many concerns [47]. In contrast, the Zn-based composites constructed in this study, which have favorable mechanical properties, and are able to generate electrical signals spontaneously, have significant potential for application in treating bone defects in load-bearing areas.

4.2. Biodegradation behavior and antibacterial performance

Ideally, bone implants should maintain their mechanical support function during the bone healing process, and then completely degrade after fulfilling their role in assisting with tissue healing. In physiological environments, Zn is mainly degraded by redox reactions. The degradation products of Zn mainly include ZnO, $Zn(OH)_2$, $Zn_3(PO_4)_2$, and trace amounts of calcium and phosphorus salts [48], which is consistent with our results (Fig. 2e). Given that the ZnO has a high solubility product constant, and is thermodynamically stable within body fluids, it effectively protects the Zn matrix, leading to a low degradation rate [22]. The complete degradation of pure Zn screws with a diameter of 5 mm may take more than ten years, which is a considerably longer period than the

3–6 months typically required for bone healing [49]. Measures to accelerate the degradation of Zn apparently need to be considered. In this study, the degradation rate of the Zn region within the Zn/Ti composites was found to be more than twice that of pure Zn (Fig. 2f). The accelerated degradation *in vivo* was also observed in the Zn region (Fig. 9a–c). As mentioned above, this accelerated degradation was attributed to the potential difference in the Zn/Ti composites, which resulted in galvanic coupling corrosion between the Zn and Ti regions.

Interestingly, a higher potential was observed in the Zn region (Fig. 1e), suggesting that initial galvanic coupling corrosion occurred with Zn serving as the cathode and Ti as the anode. Typically, in galvanic coupling corrosion, the anode corrodes preferentially due to oxidation reactions, while corrosion at the cathode is inhibited by reduction reactions [50]. However, Ti exhibits strong passivation behavior and tends to form a dense passivation film through anodic oxidation, thereby reducing its corrosion tendency. The formation of the passivation film increases the surface oxygen content of Ti, elevating its surface electrode potential and resulting in a polarity reversal of the galvanic coupling corrosion between Zn and Ti. Consequently, galvanic corrosion occurs with Zn as the anode to accelerate the degradation of Zn region. Rahimi et al. [51] observed the galvanic corrosion of Ti-Cu welded bimetal and found that after 1 h of exposure to a corrosive medium, the surface potential of Ti region increased due to the formation of Ti oxide and hydroxide. This resulted in the reversal of polar arrangement in the galvanic couples, and galvanic corrosion with Cu as the anode occurred, which was similar to our results. Considering that galvanic corrosion accelerated the degradation behavior of Zn. The rational design of Zn-based composite components will be an effective strategy to modulate the degradation of Zn. This strategy can be complemented by other measures, such as alloying and structural design, providing greater flexibility in modulating the degradation of Zn-based BMs. However, galvanic corrosion is influenced by multiple factors, including the properties and geometry of the coupling pair materials, etc. The galvanic corrosion mechanism of Zn-based composites requires further investigation, to enhance the matching between their degradation behavior and bone healing process.

The biological function of Zn-based implants depends on the concentration of Zn^{2+} released. The accelerated degradation of Zn frequently indicates an enhanced antibacterial performance [52]. In clinical treatments, implant-related infections (IRIs), which originate from bacteria adhering to implant surfaces, have consistently represented a significant challenge [53]. Severe IRIs can result in numerous complications, including chronic inflammation, pain, failure of implant function, systemic infections, and even death [54]. Zn-based implants have emerged as a promising countermeasure to IRIs, given the broad-spectrum antibacterial efficacy of Zn^{2+}. Zn^{2+} interacts with bacterial surfaces through electrostatic interactions, altering the charge balance of bacterial cell membranes, thereby leading to bacterial deformation and rupture [55]. Zn^{2+} can also interact with the thiol groups of bacterial respiratory enzymes and inhibit their function, generating reactive oxygen species (ROS) and free radicals, which in turn irreversibly damage bacterial cell membranes, DNA and mitochondria, ultimately resulting in bacterial death [56]. Moreover, the antibacterial efficacy of Zn^{2+} typically demonstrates a concentration-dependent increase [57]. In our study, an enhanced antibacterial performance was observed in Zn/Ti composites compared to pure Zn (Fig. 3). This can be attributed to the high-dose Zn^{2+} resulting from the accelerated degradation, inducing excess ROS production in the bacteria. As shown in Fig. 3f, the bacteria adhering to the surface of the Zn/Ti samples exhibited a high level of ROS formation, which validated the primary antibacterial mechanism of Zn/Ti composites. Furthermore, the voltage signal originating from the natural potential difference of the Zn/Ti composites may also contribute to enhanced antibacterial performance. It has been shown that electrical stimulation facilitates charge transfer on the surface of bacterial cell membranes, resulting in potential alterations and membrane damage, ultimately

leading to the rupture of the bacterial cell membrane [58].

4.3. Biocompatibility and osteogenic activity

Many studies have demonstrated that Zn^{2+} has a biphasic effect on osteoblasts with high concentrations of Zn^{2+} induce cell death, while low concentrations enhance cellular biological functions, including proliferation, adhesion, differentiation and biomineralization [23]. In this study, the concentrations of Zn^{2+} in the 50 % pure Zn and 30 % Zn/Ti extracts exceeded the tolerance limit of cells, causing significant cytotoxicity (Fig. 4a and b). This excess Zn^{2+} could induce an increase in intracellular ROS synthesis, leading to cellular oxidative stress, which interfered with electron transfer of uncoupled mitochondria, thereby triggering cell damage and apoptosis [59]. In the 10 % extracts, both pure Zn and Zn/Ti samples promoted the proliferation of MC3T3-E1 cells. Additionally, osteogenic differentiation of MC3T3-E1 cells was enhanced in the 30 % pure Zn and10 % Zn/Ti extracts (Fig. 5). Yu et al. [60] found that 2–5 μg/mL of Zn^{2+} induced the proliferation and differentiation of bone marrow mesenchymal stem cells via activation of the MAPK/ERK signal pathway, while 15 μg/mL of Zn^{2+} had the opposite effect. The Zn^{2+} concentrations in the 30 % pure Zn and 10 % Zn/Ti extracts were well below 15 μg/mL and close to 5 μg/mL, explaining the enhanced biological function of MC3T3-E1 cells. Unlike *in vitro* tests, the metabolic processes *in vivo* can reduce ion concentrations around implants. Referring to recommendations for *in vitro* cytotoxicity tests of BMs, extracts of Mg-based BMs were recommended to be diluted at least 6–10 times to simulate the *in vivo* environment [61]. Therefore, the *in vitro* biocompatibility of the Zn/Ti composites was guaranteed, based on the enhanced cell proliferation and differentiation in 10 % extracts.

Besides the released Zn^{2+}, the natural potential difference of Zn/Ti composites could be regarded as an intervening electrical signal (Fig. 1e and f), also exerted a positive influence on bone repair. This electrical signal exhibited a magnitude comparable to the 300 mV piezoelectricity-induced biopotential observed in bone during daily walking, which may simulate the electrical microenvironment conducive to biological functions of cells [62]. As shown in Fig. 6, the proliferation and differentiation of MC3T3-E1 cells were significantly improved by the 300 mV voltage signal. This improvement was likely attributed to the potential difference-induced electric field regulating the redistribution of charged ions and proteins on the cell membrane, and transducing external signals into the nucleus to activate the gene expression related to cell proliferation and differentiation [31]. As illustrated in Fig. 7d, activated PI3K-Akt signaling pathway was observed in the E-active group, which may be a critical signaling pathway for Zn/Ti composites to promote osteogenic differentiation through electrical signals. Studies have shown that the piezoelectric properties of piezoelectric materials could activate the cell membrane calcium channels, MAPK and PI3K-Akt signaling pathways to regulate osteogenic differentiation [62]. The intrinsic electric field of Zn/Ti composites exhibited a similar electric property, but did not necessitate mechanical stimulation. Notably, compared to the E-active group, the

activity of PI3K-Akt signaling pathway was significantly enhanced in the Zn&E-active group, which may be attributed to the up-regulated expression of the Mt1/2 genes (Fig. 7b). *Mt1/2*, as an intracellular metal-binding protein, was regulated by intracellular Zn concentration. *Mt1/2* expression will be elevated when extracellular Zn^{2+} was transported into the cell, with elevated *Mt1/2* expression in turn regulating the Zn concentration and promoting intracellular Zn homeostasis [63]. Elevated *Mt1/2* expression could also increase Akt phosphorylation, promoting the PI3K-Akt signaling pathway [64]. Therefore, under the combined effect of electrical signals and Zn^{2+}, we considered that the PI3K-Akt signaling pathway is the critical molecular mechanism by which Zn/Ti composites promote osteogenesis (Fig. 10).

Normally, the excess release of Zn^{2+} could disturb the physiological microenvironment surrounding Zn-based implants, which was unfavourable for bone repair *in vivo* [65]. However, delayed degradation could fail to match the bone repair cycle [66]. According to the *in vivo* investigation, at week 12 after the implantation, significantly improved bone healing was observed in Zn/Ti groups, compared to pure Ti and pure Zn (Figs. 8 and 9). The degradation of Zn/Ti composites *in vivo* was also higher than that of pure Zn (Fig. 9). The enhanced osteogenesis and biodegradation *in vivo* were apparently attributed to the effects of voltage signal and galvanic coupling corrosion induced by natural potential difference between Zn and Ti. Cui et al. [67] developed a novel piezoelectric polymer based on poly-L-lactic acid (PLLA), which could accelerate recruitment of stem cells during the early stage of bone repair, thereby promoting osteogenesis. Another study has also shown that electric field could modulate the polarity and directional migration of osteoblasts, facilitating their aggregation and proliferation in the defect area, and accelerating the formation of new bone tissue [68]. Based on these studies, it can be speculated that Zn/Ti composites may similarly recruit a significant number of endogenous cells *in vivo*, due to the presence of intrinsic electric field. The aggregation of endogenous cells around the implant can collectively apportion the excess Zn^{2+} released from Zn/Ti composites, thereby reducing the risk of cytotoxicity and enhancing bone regeneration.

Overall, this study demonstrates that the Zn-based composites macroscopically integrated by MMAM technology, provide significant flexibility in regulating the biodegradation and biofunctionality of Zn-based bone implants. Nevertheless, Ti is a non-biodegradable metal, and fully biodegradable components should be considered in the future scaffold designs, such as Zn/Mg composites. Also, the limitation of MMAM technology is that it only permits the printing of multimetal scaffolds with vertical or horizontal docking. The fabrication of multimetal scaffolds in the form of internal and external wrapping has not yet been realized. Further advancements in printing devices, such as the deployment of multi-laser systems and multi-powder feeding systems, may be necessary. Furthermore, how to precisely regulate the biodegradation behavior of Zn-based composites, to match the bone repair requirements in the spatio-temporal dimensions still needs to be studied in various aspects, such as component combinations, structure design and surface modification. Meanwhile, this work only reveals the comprehensive multifunctionality of MMAM Zn/Ti composites induced
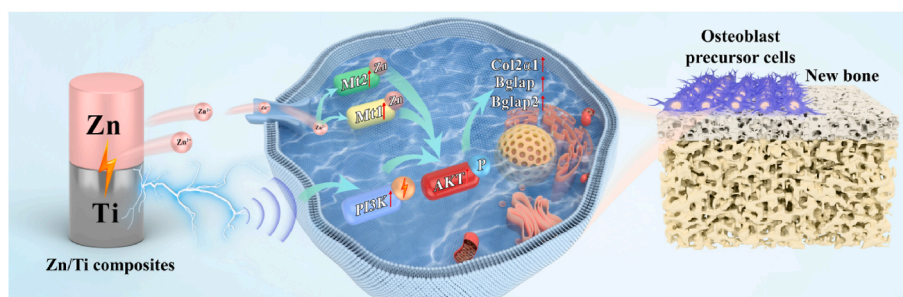

Fig. 10. Schematic diagram of the osteogenesis mechanism of Zn/Ti composites.

by the natural potential difference between Zn and Ti. We will conduct more investigations on the specific mechanism of the effect of potential difference between Zn and dissimilar metals on the degradation and biological functions of the Zn-based BMs, to boost the clinical translation of multifunctional Zn-based composites in the future.

5. Conclusion

In the present study, the Zn/Ti multimetal bone implants were successfully fabricated using MMAM technology for the first time. The microstructure, mechanical properties, surface potential, degradation behavior, antibacterial performance, and osteogenic activity were systematically investigated, and the optimization mechanism induced by natural potential difference for biodegradation and biofunction was found. The main conclusions were as follows.

(1) MMAM technology allowed the fabrication of high-quality Zn/Ti bimetal bone implants, and the refined equiaxed grains in the interfacial region endowed a strong interfacial bond between Zn and Ti. Meanwhile, a significant potential difference of 300 mV was observed between the Zn and Ti regions, which enabled the Zn/Ti composites to output a stable 300 mV voltage signal in physiological medium.

(2) Both the *in vitro* and *in vivo* degradation rate of the Zn region in Zn/Ti composites were significantly accelerated compared to pure Zn, since the galvanic coupling corrosion triggered by the potential difference between Zn and Ti regions. Additionally, the accelerated degradation resulted in the release of a large amount of Zn^{2+}, thereby enhancing the antibacterial performance of Zn/Ti composites.

(3) The Zn/Ti composites could activate the PI3K-Akt signaling pathway through the synergistic effect of released Zn^{2+} and voltage signal, promoting the proliferation and osteogenic differentiation of MC3T3-E1 cells. In situ implantation of Zn/Ti composites in a femoral condylar defect model also verified their ability to induce bone repair *in vivo*, confirming their potential as implants for treating bone defects.

CRediT authorship contribution statement

Jing Xu: Writing – original draft, Investigation, Data curation, Conceptualization. **Zhenbao Zhang:** Writing – original draft, Investigation, Data curation, Conceptualization. **Jianhui Wang:** Investigation, Data curation. **Yuhan Qi:** Investigation, Data curation. **Xiaohong Qi:** Methodology. **Yijie Liang:** Investigation. **Manxi Li:** Investigation. **Haixia Li:** Software. **Yantao Zhao:** Supervision, Resources. **Zhuangzhuang Liu:** Writing – review & editing, Supervision, Resources. **Yanfeng Li:** Writing – review & editing, Supervision, Resources.

Data availability

The data that support the findings of this article are available from the corresponding author upon reasonable request.

Ethics approval and consent to participate

All animal operations were approved by the Animal Ethics Committee of the Beijing Keyu Animal Breeding Center (KY20230426002).

Declaration of competing interest

The authors declare that they have no known competing financial interests or personal relationships that could have appeared to influence the work reported in this paper.

Appendix A. Supplementary data

Supplementary data to this article can be found online at https://doi.org/10.1016/j.bioactmat.2024.10.030.

References

[1] P.W. Kämmerer, B. Al-Nawas, Bone reconstruction of extensive maxillomandibular defects in adults, Periodontol 2023 93 (1) (2000) 340–357.

[2] L. Impieri, A. Pezzi, H. Hadad, G.M. Peretti, L. Mangiavini, N. Rossi, Orthobiologics in delayed union and non-union of adult long bones fractures: a systematic review, BoneKEy Rep. 21 (2024) 101760.

[3] G.W. Qian, T.T. Wu, Z.Z. Wang, B. Yu, J.D. Ye, Synergistic effects of calcium silicate/zinc silicate dual compounds andin-situinterconnected pores on promoting bone regeneration of composite scaffolds, Biomed. Mater. 19 (3) (2024) 035024.

[4] M.H. Wu, M.H. Lee, C. Wu, P.I. Tsai, W.B. Hsu, S.I. Huang, T.H. Lin, K.Y. Yang, C. Y. Chen, S.H. Chen, C.Y. Lee, T.J. Huang, F.H. Tsau, Y.Y. Li, *In vitro* and *in vivo* comparison of bone growth characteristics in additive-manufactured porous titanium, nonporous titanium, and porous tantalum interbody cages, Materials 15 (10) (2022) 3670.

[5] M. Li, M.W. Jiang, Y. Gao, Y.F. Zheng, Z. Liu, C. Zhou, T. Huang, X.N. Gu, A. Li, J. C. Fang, X.M. Ji, Current status and outlook of biodegradable metals in neuroscience and their potential applications as cerebral vascular stent materials, Bioact. Mater. 11 (2021) 140–153.

[6] H.T. Yang, X.H. Qu, M.Q. Wang, H.W. Cheng, B. Jia, J.F. Nie, K.R. Dai, Y.F. Zheng, Zn-0.4Li alloy shows great potential for the fixation and healing of bone fractures at load-bearing sites, Chem. Eng. J. 417 (2021) 129317.

[7] Z.C. Zhang, B. Jia, H.T. Yang, Y. Han, Q. Wu, K.R. Dai, Y.F. Zheng, Zn0.8Li0.1Sr-a biodegradable metal with high mechanical strength comparable to pure Ti for the treatment of osteoporotic bone fractures: *In vitro* and *in vivo* studies, Biomaterials 275 (2021) 120905.

[8] H. Guo, D.D. Xia, Y.F. Zheng, Y. Zhu, Y.S. Liu, Y.S. Zhou, A pure zinc membrane with degradability and osteogenesis promotion for guided bone regeneration: *In vitro* and *in vivo* studies, Acta Biomater. 106 (2020) 396–409.

[9] Z.C. Zhang, B. Jia, H.T. Yang, Y. Han, Q. Wu, K.R. Dai, Y.F. Zheng, Biodegradable ZnLiCa ternary alloys for critical-sized bone defect regeneration at load-bearing sites: *In vitro* and *in vivo* studies, Bioact. Mater. 6 (11) (2021) 3999–4013.

[10] Y.W. Yang, M.L. Yang, C.X. He, F.W. Qi, D. Wang, S.P. Peng, C.J. Shuai, Rare earth improves strength and creep resistance of additively manufactured Zn implants, Compos part B-Eng 216 (2021) 108882.

[11] P. Li, J.T. Dai, Y.G. Li, D. Alexander, J. Čapek, J. Geis-Gerstorfer, G.J. Wan, J. M. Han, Z.T. Yu, A. Li, Zinc based biodegradable metals for bone repair and regeneration: bioactivity and molecular mechanisms, Mater Today Bio 25 (2023) 100932.

[12] M.X. Wang, X. Zhou, Y.H. Li, Y.Q. Dong, J.S. Meng, S. Zhang, L.B. Xia, Z.Z. He, L. Ren, Z.W. Chen, X.C. Zhang, Triple-synergistic MOF-nanozyme for efficient antibacterial treatment, Bioact. Mater. 17 (2022) 289–299.

[13] R. Davis, A. Singh, M.J. Jackson, R.T. Coelho, D. Prakash, C.P. Charalambous, W. Ahmed, Lrr da Silva, A.A. Lawrence, A comprehensive review on metallic implant biomaterials and their subtractive manufacturing, Int. J. Adv. Manuf. Technol. 120 (3–4) (2022) 1473–1530.

[14] Y. Zhou, J.W. Wang, Y.W. Yang, M.L. Yang, H.Z. Zheng, D.Q. Xie, D.S. Wang, L. D. Shen, Laser additive manufacturing of zinc targeting for biomedical application, Int J Bioprinz 8 (1) (2022) 501.

[15] S. Chowdhury, N. Yadaiah, C. Prakash, S. Ramakrishna, S. Dixit, L.R. Gupta, D. Buddhi, Laser powder bed fusion: a state-of-the-art review of the technology, materials, properties & defects, and numerical modelling, J. Mater. Res. Technol. 20 (2022) 2109–2172.

[16] D.D. Xia, Y. Qin, H. Guo, P. Wen, H. Lin, M. Voshage, J.H. Schleifenbaum, Y. Cheng, Y.F. Zheng, Additively manufactured pure zinc porous scaffolds for critical-sized bone defects of rabbit femur, Bioact. Mater. 19 (2022) 12–23.

[17] X. Wang, A.B. Liu, Z.B. Zhang, D.Z. Hao, Y.J. Liang, J.B. Dai, X. Jin, H.Z. Deng, Y. T. Zhao, P. Wen, Y.F. Li, Additively manufactured Zn-2Mg alloy porous scaffolds with customizable biodegradable performance and enhanced osteogenic ability, Adv. Sci. 11 (5) (2024) 2307329.

[18] A.B. Liu, Y.P. Lu, J.B. Dai, P. Wen, D.D. Xia, Y.F. Zheng, Mechanical properties, *in vitro* biodegradable behavior, biocompatibility and osteogenic ability of additively manufactured Zn-0.8Li-0.1Mg alloy scaffolds, Biomater. Adv. 153 (2023) 213571.

[19] X. Tong, D.H. Zhang, X.T. Zhang, Y.C. Su, Z.M. Shi, K. Wang, J.G. Lin, Y.C. Li, JXg Lin, C.E. Wen, Microstructure, mechanical properties, biocompatibility, and *in vitro* corrosion and degradation behavior of a new Zn-5Ge alloy for biodegradable implant materials, Acta Biomater. 82 (2018) 197–204.

[20] Y. Qin, A.B. Liu, H. Guo, Y.N. Shen, P. Wen, H. Lin, D.D. Xia, M. Voshage, Y. Tian, Y.F. Zheng, Additive manufacturing of Zn-Mg alloy porous scaffolds with enhanced osseointegration: *In vitro* and *in vivo* studies, Acta Biomater. 145 (2022) 403–415.

[21] A.J. Drelich, S. Zhao, R.J. Guillory, J.W. Drelich, J. Goldman, Long-term surveillance of zinc implant in murine artery: surprisingly steady biocorrosion rate, Acta Biomater. 58 (2017) 539–549.

[22] H.T. Yang, C. Wang, C.Q. Liu, H.W. Chen, Y.F. Wu, J.T. Han, Z.C. Jia, W.J. Lin, D. Y. Zhang, W.T. Li, W. Yuan, H. Guo, H.F. Li, G.X. Yang, D.L. Kong, D.H. Zhu, K. Takashima, L.Q. Ruan, J.F. Nie, X. Li, Y.F. Zheng, Evolution of the degradation mechanism of pure zinc stent in the one-year study of rabbit abdominal aorta model, Biomaterials 145 (2017) 92–105.

[23] Z.B. Zhang, A.B. Liu, J.D. Fan, M.L. Wang, J.B. Dai, X. Jin, H.Z. Deng, X. Wang, Y. J. Liang, H.X. Li, Y.T. Zhao, P. Wen, Y.F. Li, A drug-loaded composite coating to improve osteogenic and antibacterial properties of Zn-1Mg porous scaffolds as biodegradable bone implants, Bioact. Mater. 27 (2023) 488–504.

[24] Y.T. Zhu, K. Ameyama, P.M. Anderson, I.J. Beyerlein, H.J. Gao, H.S. Kim, E. Lavernia, S. Mathaudhu, H. Mughrabi, R.O. Ritchie, N. Tsuji, X.Y. Zhang, X. L. Wu, Heterostructured materials: superior properties from hetero-zone interaction, Mater Res Lett 9 (1) (2020) 1–31.

[25] L. Romero-Resendiz, M. El-Tahawy, T. Zhang, M.C. Rossi, D.M. Marulanda-Cardona, T. Yang, V. Amigó-Borrás, Y. Huang, H. Mirzadeh, I.J. Beyerlein, J. C. Huang, T.G. Langdon, Y.T. Zhu, Heterostructured stainless steel: properties, current trends, and future perspectives, Mater. Sci. Eng., A R 150 (2022) 100691.

[26] Q.X. Sun, D.C. Zhang, X. Tong, J.G. Lin, Y.C. Li, C.E. Wen, Mechanical properties, corrosion behavior, and cytotoxicity of biodegradable Zn/Mg multilayered composites prepared by accumulative roll bonding process, Acta Biomater. 173 (2024) 509–525.

[27] T.Y. Zheng, Y.Y. Pang, D.X. Zhang, Y. Wang, X. Zhang, H.J. Leng, Y.J. Yu, X. P. Yang, Q. Cai, Integrated piezoelectric/conductive composite cryogel creates electroactive microenvironment for enhanced bone regeneration, Adv. Healthcare Mater. 12 (26) (2023) e2300927.

[28] S.Y. Luo, C.S. Zhang, W. Xiong, Y.P. Song, Q. Wang, H.Z. Zhang, S. Guo, S.D. Yang, H.Y. Liu, Advances in electroactive biomaterials: through the lens of electrical stimulation promoting bone regeneration strategy, J Orthop Translat 47 (2024) 191–206.

[29] T. Jiang, F. Yu, Y.Q. Zhou, R.M. Li, M.T. Zheng, Y.Y. Jiang, Z.X. Li, J. Pan, N. J. Ouyang, Synergistic effect of ultrasound and reinforced electrical environment by bioinspired periosteum for enhanced osteogenesis via immunomodulation of macrophage polarization through Piezo1, Mater Today Bio 27 (2024) 101147.

[30] C.C. Yu, X.Z. Ying, M.A. Shahbazi, L.J. Yang, Z.Q. Ma, L. Ye, W.T. Yang, R.T. Sun, T.Y. Gu, R.K. Tang, S.W. Fan, S.S. Yao, A nano-conductive osteogenic hydrogel to locally promote calcium influx for electro-inspired bone defect regeneration, Biomaterials 301 (2023) 122266.

[31] S.T. Chen, Y. Li, S.Y. He, P. Zhou, J. Lu, N. Gu, Microscopic Volta potential difference on metallic surface promotes the osteogenic differentiation and proliferation of human mesenchymal stem cells, Mater. Sci. Eng., C 128 (2021) 112325.

[32] A. Verma, A. Kapil, D. Klobčar, A. Sharma, A review on multiplicity in multi-material additive manufacturing: process, capability, scale, and structure, Materials 16 (15) (2023) 5246.

[33] I. Meyer, M. Oel, T. Ehlers, R. Lachmayer, Additive manufacturing of multi-material parts - design guidelines for manufacturing of 316L/CuCrZr in laser powder bed fusion, Heliyon 9 (8) (2023) e18301.

[34] H.Y. Shi, P. Zhou, J. Li, C.Z. Liu, L.Q. Wang, Functional gradient metallic biomaterials: techniques, current scenery, and future prospects in the biomedical field, Front. Bioeng. Biotechnol. 8 (2021) 616845.

[35] F. Bartolomeu, O. Carvalho, M. Gasik, F.S. Silva, Multi-functional Ti6Al4V-CoCrMo implants fabricated by multi-material laser powder bed fusion technology: a disruptive material's design and manufacturing philosophy, J. Mech. Behav. Biomed. Mater. 138 (2023) 105583.

[36] Y. Zhou, L.C. Duan, F. Li, K.Y. Chen, S.F. Wen, Effect of heat treatment on the microstructure and mechanical property of W/316L multi-material fabricated by selective laser melting, J. Alloys Compd. 890 (2022) 161841.

[37] H. Hotz, M. Zimmermann, S. Greco, B. Kirsch, J.C. Aurich, Additive manufacturing of functionally graded Ti-Al structures by laser-based direct energy deposition, J. Manuf. Process. 68 (2021) 1524–1534.

[38] L.D. Bobbio, R.A. Otis, J.P. Borgonia, R.P. Dillon, A.A. Shapiro, Z.K. Liu, A. M. Beese, Additive manufacturing of a functionally graded material from Ti-6Al-4V to Invar: experimental characterization and thermodynamic calculations, Acta Mater. 127 (2017) 133–142.

[39] P. Wen, L. Jauer, M. Voshage, Y.Z. Chen, R. Poprawe, J.H. Schleifenbaum, Densification behavior of pure Zn metal parts produced by selective laser melting for manufacturing biodegradable implants, J. Mater. Process. Technol. 258 (2018) 128–137.

[40] E. Davoodi, H. Montazerian, A.S. Mirhakimi, M. Zhianmanesh, O. Ibhadode, S. I. Shahabad, R. Esmaeilizadeh, E. Sarikhani, S. Toorandaz, S.A. Sarabi, R. Nasiri, Y. Z. Zhu, J. Kadkhodapour, B.B. Li, A. Khademhosseini, E. Toyserkani, Additively manufactured metallic biomaterials, Bioact. Mater. 15 (2022) 214–249.

[41] Y.W. Yang, Y. Cheng, S.P. Peng, L. Xu, C.X. He, F.W. Qi, M.C. Zhao, C.J. Shuai, Microstructure evolution and texture tailoring of reduced graphene oxide reinforced Zn scaffold, Bioact. Mater. 6 (5) (2021) 1230–1241.

[42] P. Peljo, J.A. Manzanares, H.H. Girault, Contact potentials, fermi level equilibration, and surface charging, Langmuir 32 (23) (2016) 5765–5775.

[43] Z.F. Yin, M.L. Yan, Z.Q. Bai, W.Z. Zhao, W.J. Zhou, Galvanic corrosion associated with SM 80SS steel and Ni-based alloy G3 couples in NaCl solution, Electrochim. Acta 53 (22) (2008) 6285–6292.

[44] Q.Y. Li, H. Lu, J. Cui, M.Z. An, D.Y. Li, Understanding the low corrosion potential and high corrosion resistance of nano-zinc electrodeposit based on electron work function and interfacial potential difference, RSC Adv. 6 (100) (2016) 97606–97612.

[45] F. Ali, M. Koc, 3D printed polymer piezoelectric materials: transforming healthcare through biomedical applications, Polymers 15 (23) (2023) 4470.

[46] D. Khare, B. Basu, A.K. Dubey, Electrical stimulation and piezoelectric biomaterials for bone tissue engineering applications, Biomaterials 258 (2020) 120280.

[47] A. Nain, S. Chakraborty, S.R. Barman, P. Gavit, S. Indrakumar, A. Agrawal, Z. H. Lin, K. Chatterjee, Progress in the development of piezoelectric biomaterials for tissue remodeling, Biomaterials 307 (2024) 122528.

[48] I. Cockerill, Y.C. Su, S. Sinha, Y.X. Qin, Y.F. Zheng, M.L. Young, D.H. Zhu, Porous zinc scaffolds for bone tissue engineering applications: a novel additive manufacturing and casting approach, Mat Sci Eng C-Mater 110 (2022) 110738.

[49] H.T. Yang, X.H. Qu, W.J. Lin, C. Wang, D.H. Zhu, K.R. Dai, Y.F. Zheng, *In vitro* and *in vivo* studies on zinc-hydroxyapatite composites as novel biodegradable metal matrix composite for orthopedic applications, Acta Biomater. 71 (2018) 200–214.

[50] D.Q. Ng, J.K. Lin, Y.P. Lin, Lead release in drinking water resulting from galvanic corrosion in three-metal systems consisting of lead, copper and stainless steel, J. Hazard Mater. 398 (2020) 122936.

[51] E. Rahimi, A. Rafsanjani-Abbasi, A. Imani, S. Hosseinpour, A. Davoodi, Insights into galvanic corrosion behavior of Ti-Cu dissimilar joint: effect of microstructure and volta potential, Materials 11 (10) (2018) 1820.

[52] Z.J. He, C. Jiao, J.N. Wu, J.S. Gu, H.X. Liang, L.D. Shen, Y.W. Yang, Z.J. Tian, C. J. Wang, Q. Jiang, Zn-doped chitosan/alginate multilayer coatings on porous hydroxyapatite scaffold with osteogenic and antibacterial properties, Int J Bioprint 9 (2) (2023) 668.

[53] N.L. Yang, X.Y. Yang, S.N. Cheng, X. Gao, S.M. Sun, X. Huang, J. Ge, Z.H. Han, C. Huang, Y.J. Wang, C. Cheng, L. Cheng, Magnesium implants with alternating magnetic field-enhanced hydrogen release and proton depletion for anti-infection treatment and tissue repair, Bioact. Mater. 38 (2024) 374–383.

[54] X.G. Chen, J.H. Zhou, Y. Qian, L.Z. Zhao, Antibacterial coatings on orthopedic implants, Mater Today Bio 19 (2023) 100586.

[55] L.L. Wang, C. Hu, L.Q. Shao, The antimicrobial activity of nanoparticles: present situation and prospects for the future, Int. J. Nanomed. 12 (2017) 1227–1249.

[56] S. Gharpure, B. Ankamwar, Synthesis and antimicrobial properties of zinc oxide nanoparticles, J. Nanosci. Nanotechnol. 20 (10) (2020) 5977–5996.

[57] J. He, J. Fang, P.B. Wei, Y.L. Li, H. Guo, Q.S. Mei, F.Z. Ren, Cancellous bone-like porous Fe@Zn scaffolds with core-shell-structured skeletons for biodegradable bone implants, Acta Biomater. 121 (2021) 665–681.

[58] N. Zhang, X.W. Zhang, Y.Y. Zhu, D. Wang, W. Liu, D. Chen, R. Li, S.X. Li, MOF/MXene-loaded PVA/chitosan hydrogel with antimicrobial effect and wound healing promotion under electrical stimulation and improved mechanical properties, Int. J. Biol. Macromol. 264 (Pt 2) (2024) 130625.

[59] X. Jin, D.X. Xie, Z.B. Zhang, A.B. Liu, M.L. Wang, J.B. Dai, X. Wang, H.Z. Deng, Y. J. Liang, Y.T. Zhao, P. Wen, Y.F. Li, *In vitro* and *in vivo* studies on biodegradable Zn porous scaffolds with a drug-loaded coating for the treatment of infected bone defect, Mater Today Bio 24 (2023) 100885.

[60] Y.Q. Yu, K. Liu, Z. Wen, W.C. Liu, L. Zhang, J.S. Su, Double-edged effects and mechanisms of Zn^{2+} microenvironments on osteogenic activity of BMSCs: osteogenic differentiation or apoptosis, RSC Adv. 10 (25) (2020) 14915–14927.

[61] J.L. Wang, F. Witte, T.F. Xi, Y.F. Zheng, K. Yang, Y.S. Yang, D.W. Zhao, J. Meng, Y. D. Li, W.R. Li, K.M. Chan, L. Qin, Recommendation for modifying current cytotoxicity testing standards for biodegradable magnesium-based materials, Acta Biomater. 21 (2015) 237–249.

[62] S.Q. Zhou, C.R. Xiao, L. Fan, J.H. Yang, R.H. Ge, M. Cai, K.T. Yuan, C.H. Li, R. W. Crawford, Y. Xiao, P. Yu, C.L. Deng, C.Y. Ning, L. Zhou, Y. Wang, Injectable ultrasound-powered bone-adhesive nanocomposite hydrogel for electrically accelerated irregular bone defect healing, J. Nanobiotechnol. 22 (1) (2024) 54.

[63] A.I. Abdo, H.B. Tran, S. Hodge, J.F. Beltrame, P.D. Zalewski, Zinc homeostasis alters zinc transporter protein expression in vascular endothelial and smooth muscle cells, Biol. Trace Elem. Res. 199 (6) (2021) 2158–2171.

[64] E. Vergadi, E. Ieronymaki, K. Lyroni, K. Vaporidi, C. Tsatsanis, Akt signaling pathway in macrophage activation and M1/M2 polarization, J. Immunol. 198 (3) (2017) 1006–1014.

[65] J.L. Xu, G. Bao, B. Jia, M.Q. Wang, P. Wen, T.Y. Kan, S.T. Zhang, A.B. Liu, H. Z. Tang, H.T. Yang, B. Yue, Kerong Dai, Y.F. Zheng, X.H. Qu, An adaptive biodegradable zinc alloy with bidirectional regulation of bone homeostasis for treating fractures and aged bone defects, Bioact. Mater. 38 (2024) 207–224.

[66] Y.X. Shi, Z. Xue, P. Li, S. Yang, D.W. Zhang, S.X. Zhou, Z.P. Guan, Y.G. Li, L. N. Wang, Surface modification on biodegradable zinc alloys, J. Mater. Res. Technol. 25 (2023) 3670–3687.

[67] X. Cui, L.L. Xu, Y.Z. Shan, J.X. Li, J.Y. Ji, E.G. Wang, B.K. Zhang, X.Z. Wen, Y. Bai, D. Luo, C.Y. Chen, Z. Li, Piezocatalytically-induced controllable mineralization scaffold with bone-like microenvironment to achieve endogenous bone regeneration, Sci. Bull. 69 (12) (2024) 1895–1908.

[68] M. Rohde, J. Ziebart, T. Kirschstein, T. Sellmann, K. Porath, F. Kühl, B. Delenda, C. Bahls, U.V. Rienen, R. Bader, R. Köhling, Human osteoblast migration in DC electrical fields depends on store operated Ca^{2+}-release and is correlated to upregulation of stretch-activated TRPM7 channels, Front. Bioeng. Biotechnol. 7 (2019) 422.